

Experimental Investigation of Mean and Turbulent Characteristics of a Free Air Rectangular Jet with/without Lip Length

Youssef Gamal Nasr Ahmed (يوسف جمال نصر أحمد)^{a,c}, Reza Alidoost Dafsari (رضا علي دوست دافساري)^b, and Jeekeun Lee (이재근)^{a,b*}

^a Division of Mechanical Aerospace Electrical Convergence Engineering, Jeonbuk National University, Jeonju 54896, Republic of Korea

^b Department of Mechanical System Engineering, Jeonbuk National University, Jeonju 54896, Republic of Korea

^c Department of Mechanical Power Engineering and Energy, Faculty of Engineering, Minia University, El-Minia, 61519, Egypt

* Email: leejk@jbnu.ac.kr

Abstract

The influence of geometric modifications to a rectangular nozzle on the flow structure of a free jet was investigated experimentally. In this work, an adaptable nozzle was employed, featuring exchangeable upper and lower plates that could be replaced to achieve the desired lip length, while the remaining geometry was unchanged. This study aims to assess the effect of lip length on flow structure, by comparing a nozzle with equal lip length, serving as a reference, to configurations with 10 and 20 mm lower lip extensions. Both the mean and turbulent properties of the jet were characterized along the streamwise and spanwise directions using a 2-dimensional hot-wire system. In addition, Particle Image Velocimetry (PIV) was utilized for flow visualization, assessment of air entrainment, and Proper Orthogonal Decomposition (POD) analysis. The findings indicate that increasing the lip length broadens the radial spread of the mean axial and radial velocity distributions and amplifies velocity fluctuations, resulting in enhanced mixing. Furthermore, a longer lip increases the centerline velocity decay rate and enhances velocity fluctuations along the centerline, producing a reduced potential core length relative to the equal-length configuration. It also produces a wider shear stress distribution and increases the turbulent transport of normal and shear stresses via radial velocity fluctuations. PIV imaging and POD analysis further demonstrated asymmetric vortex roll-up and mixing with ambient fluid. The newly explored lip length effect has potential applications in flow control and could be relevant to a wide range of industrial free turbulent jet technologies.

Keywords: Constant Temperature hotwire Anemometry (CTA), Flow control, Free Jet, PIV visualization, POD analysis, Rectangular nozzle, Turbulent Jet, Unsteady analysis.

1. Introduction

Free jets play a critical role in a variety of industrial contexts within mechanical, chemical, and aerospace engineering, making them an important topic for extensive research. Such jets emerge from a nozzle into an open environment, where they entrain ambient fluid and expand radially as they advance downstream ¹⁻³. The evolution of the flow field is influenced by both initial and boundary conditions ⁴⁻⁸. Efficient mixing and entrainment of the surrounding fluid are vital for the effectiveness of propulsion systems, combustion

36 processes, chemical reactors, and environmental engineering applications. Turbulent free jets have been
 37 investigated with both axisymmetric and non-axisymmetric nozzle designs, and prior studies have shown that

AR	nozzle-exit aspect ratio, AR=w/h	U_{rms}	root-mean-square of axial velocity
A_sR	asymmetric ratio, $A_sR = (A^+ - A^-) / (A^+ + A^-)$, A^+ calculated at positive $y/y_{0.5}$, A^- calculated at negative $y/y_{0.5}$	$u'v'$	fluctuation, m/s
h	height of the nozzle, m	$u'u'v'$	Reynolds shear stress, m^2/s^2
L	height of the nozzle, m	$u'v'v'$	turbulent transport of Reynolds normal stress ($u'v'$) by the cross-stream velocity fluctuation (v'), m^3/s^3
P_c	potential core length, m	V_{rms}	turbulent transport of Reynolds shear stress ($u'v'$) by cross-stream velocity fluctuation (v'), m^3/s^3
Q	volume flow rate, m^3/s	V_{or}	root-mean-square of radial velocity fluctuation, m/s
Q_x^*	nondimensional volume flow rate at any axial position, Q_o^* at the exit, air entrainment Q_e^*	V	virtual origin, m
Re_h	Reynolds number based on nozzle height (h), $Re_h = U_0 h / \mu$	w	mean radial velocity, m/s
SR_y	jet spreading rate	$y_{0.5}$	nozzle width, m
U_o	mean centerline exit velocity, m/s		half-width, defined as the y-location where $U(x) = 0.5 U_c(x)$, m
U_c	mean axial centerline velocity, m/s		

38 non-axisymmetric jets generally provide superior mixing with ambient fluid compared to axisymmetric jets ^{9–}
 39 ¹¹. Rectangular (non-axisymmetric) jets are advantageous due to their straightforward design and ease of
 40 manufacture. They are now widely recognized as among the most frequently employed components in
 41 propulsion systems for both spacecraft and airplanes ¹². The design of rectangular nozzles is frequently adapted
 42 for flow control to tailor the jet structure in both near and far fields, depending on the performance needs of
 43 the application. The rectangular nozzle's aspect ratio (AR , defined as width/height) significantly affects flow
 44 behavior, specifically influencing whether the resulting flow is 3D or 2D. A 2D (two-dimensional) jet flow
 45 occurs when the fluid velocity and flow characteristics change mainly in two spatial directions, while the third
 46 (spanwise) direction features minimal or uniform variation. In comparison, 3D rectangular jet flows include
 47 significant axial, radial, and spanwise velocity components, all of which shape the complex flow structure.
 48 Rectangular nozzles with a lower AR produce jet structures exhibiting greater three-dimensionality, typified
 49 by prominent ring-like 3D vortices, whereas higher AR nozzles generate more 2D roller-like vortices ¹³.
 50 Depending on the AR , there exists a 2-D region that influences ambient entrainment in the spanwise direction.
 51 The evolution of a rectangular jet flow is defined by the presence of a potential core region ($U_c \approx 0.98U_o$), a
 52 region where centerline velocity decays ($U_c \sim x^{-0.5}$), and an axisymmetric region ($U_c \sim x^{-1}$) ^{13–23}. Several
 53 parameters are critical for the control of turbulent free jet flows: aspect ratio, Reynolds number (Re), the
 54 presence or absence of sidewalls, presence or absence of endplates, and the geometric details of the nozzle
 55 exit.

56 The influence of various AR values in a rectangular jet has been thoroughly studied. Studies have reported that
 57 the extent of the 2-D region expands as AR increases ^{3,14,17,21}. Deo et al. ²⁴ observed that a greater aspect ratio
 58 leads to a longer potential core, conflicting with the results reported by Sforza et al. ¹⁷. Quinn ²⁵ demonstrated
 59 that, with increasing slot aspect ratio, the mixing process in the near-field accelerates, and the far-field mean
 60 axial velocity decay rates also become more pronounced. The region governed by power-law decay and jet

spreading increases as AR rises, whereas both the entrainment rate and the distance required for achieving self-similarity decrease, according to Deo et al.²⁴. Tsuchiya and Horikoshi²⁶ reported that the axial turbulence intensity increases downstream for high aspect ratio jets; however, it decreases as Reynolds number rises. Findings by Krothapalli et al.¹⁹ indicated that, at a location approximately 30h downstream from the nozzle, aspect ratio does not affect mean velocity and shear stress distributions along both axial and radial directions.

Numerous research studies have investigated how mean and turbulent flow characteristics depend on the Reynolds number. Hussain and Clark²⁷ demonstrated that the centerline mean velocity decay, the kinematic and geometric virtual origin, and the jet width rate were significantly affected by the initial conditions. The longitudinal shear layer turbulence intensity peaks are lower when the initial flow is turbulent compared to a laminar flow. For low Reynolds numbers, Lemieux and Oosthuizen²⁸ showed that the exit Reynolds number did not influence the mean velocity profiles. However, it had a significant impact on the centerline velocity decay rate and the turbulence stress levels. As the Reynolds number increases, turbulence stresses in the central jet region become higher, yet the spread rate and longitudinal normal turbulence stress levels are only slightly changed. Namer and Ötügen²⁹ observed that the Reynolds number does not affect the average size or the number of large-scale turbulence structures (per unit length of jet). Although the boundary layer thickness slightly increases as Reynolds number decreases, higher Reynolds numbers are correlated with lower jet diffusion and spread rates. Findings by Deo et al.³⁰ indicate that the potential core length shortens with increasing Re , while the near field spreading rate increases. In a separate study by Deo et al.³¹, it was found that as Re rises, the velocity profiles in the near field become increasingly flat. The axial distance causes both mass flow rates and momentum thicknesses to increase linearly, but the rate of increase diminishes as Re grows. Ghasemi et al.¹¹ reported a thicker shear layer at low Re numbers; however, further increases in Re number beyond a certain threshold do not change the shear layer thickness.

Hitchman et al.³² demonstrated that the inclusion of sidewalls (two parallel plates attached to the short sides of the nozzle) enhances the decay rate, suppresses the spread rate, and diminishes the kinematic momentum flux. Deo et al.¹⁴ identified that the use of sidewalls leads to an extended potential core and 2-D region, as well as reduced decay and spread rates. Nonetheless, the near-field vortex shedding rate displays a decrease in dominant shedding frequency and an increase in frequency peaks. Alnahhal and Panidis¹⁵ showed that, in the near field, the outer region of the jet with sidewalls exhibited an increased mean axial velocity and a reduced outward radial mean velocity. The existence of distinct 2D roller structures also produces pronounced peaks in the skewness factor at the periphery of the jet. Alnahhal et al.³³ reported that, in the absence of sidewalls, the existence or lack of an endplate does not alter the flow field evolution. However, when sidewalls are present, elevated axial velocities at the jet edge and reduced transverse velocities in the radial direction are observed. It has been indicated that axial rms velocity distributions require a greater axial distance to reach self-similarity when sidewalls are present^{15,33}.

Bridges and Wernet³⁴ performed a comprehensive experimental study to compare the mean flow and turbulence features of round, rectangular, and bevelled rectangular nozzles. The height and width of the nozzles

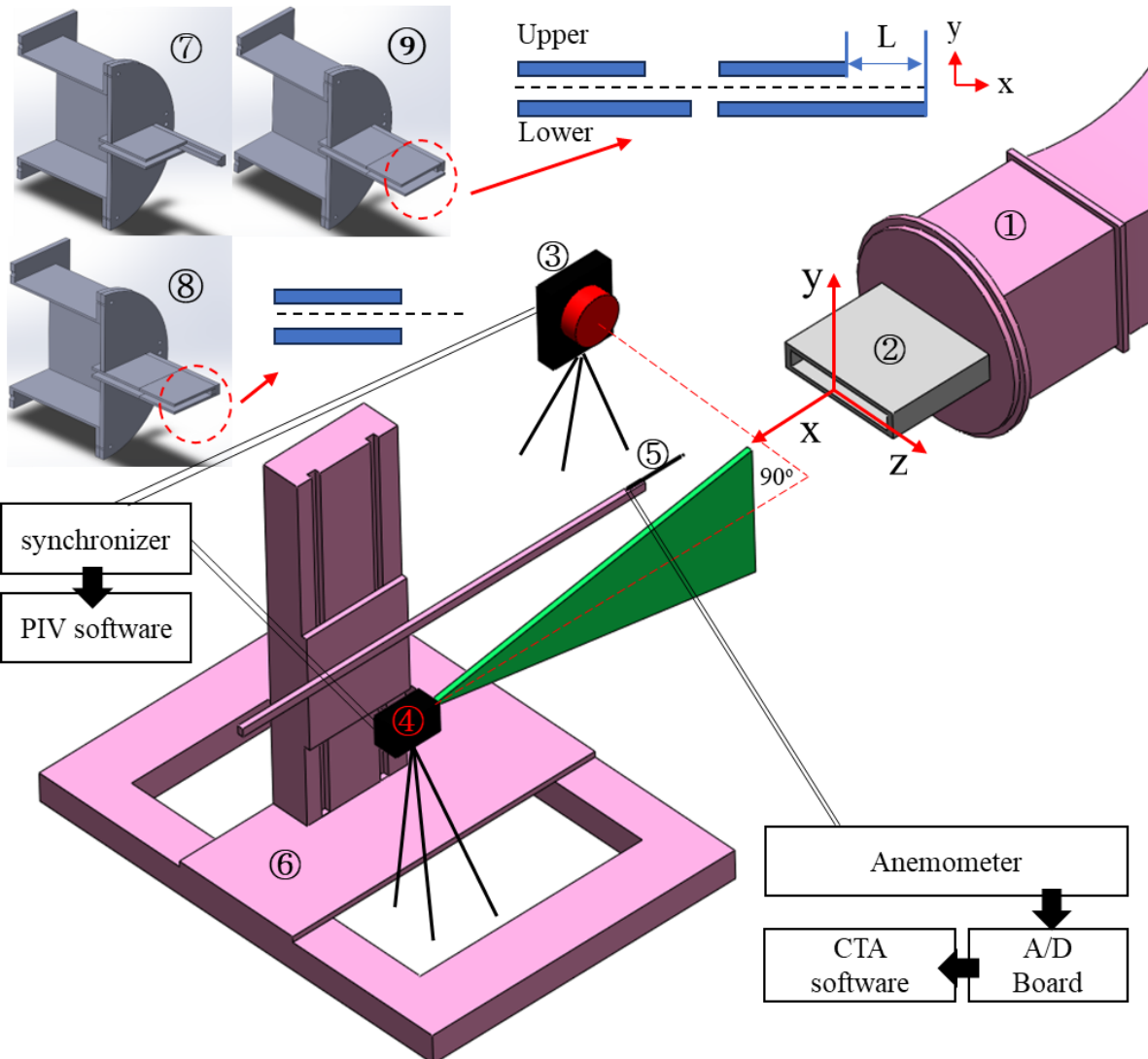
defined an equivalent diameter (D_j) of 2.14 inches (54.5 mm), and three aspect ratios were examined: 2:1, 4:1, and 8:1. Bevelled configurations with two distinct extension lengths were manufactured for each aspect ratio, along with standard rectangular nozzles. The length of the potential core decreased from $x/D_j = 7.8$ for the round jet to $x/D_j = 6$, $x/D_j = 4$, and $x/D_j = 3$ for rectangular jets with aspect ratios of 2:1, 4:1, and 8:1, respectively. For the larger aspect ratio rectangular nozzles, the peak variance of axial components was slightly higher than that found for the round jet, varying from 0.016 (8:1) to 0.019 (2:1), while the round jet exhibited a value of 0.016. Analysis of the bevelled rectangular nozzles reveals that the shear layer initiates later on the long side of the bevelled nozzle, while for the 2:1 aspect ratio, the difference is minimal compared to the standard rectangular nozzle. Altering the bevelled rectangular nozzle's aspect ratio influences the flow properties near the jet centerline. The variance of the axial component increases more rapidly and reaches its peak sooner than the standard value along the centerline, with a 30% rise noted at the lipline for the shorter extension and a 75% rise for the longer extension.

Limited studies have examined how lip length affects flow behaviour in nozzles. The results obtained by Kiwata³⁵ et al. for a rectangular nozzle with a geometry similar to this study and a velocity of 7 m/s revealed that extending the lower lip-plate considerably alters the flow characteristics. Increased lip-plate length (L/h) from 0 to 8 led to enhanced jet entrainment and spreading, with the most notable improvement seen at a moderate L/h ratio of 2. Hirata et al.³⁶ investigated the influence of lip length for a rectangular nozzle with aspect ratio 300 and Re of 6000. The nozzle's upper lip lengths were 2h, 3.3h, and 5h (where h, or nozzle exit height, was 1.5 mm), and greater lip length corresponded to decreased plate thickness. Their findings demonstrated that potential core length remains unaffected by lip length, while the normalized flow rate increases in the downstream direction as lip length becomes larger. Asymmetry in lip length was found to substantially influence the velocity distribution and spreading patterns of the jet. Nevertheless, the author pointed out the challenges in comprehensively understanding the flow behaviour associated with nozzle modification.

While substantial research exists on rectangular and asymmetric nozzles, the literature still lacks a thorough exploration of rectangular nozzles featuring extended lip lengths. Prior work has primarily addressed the aerodynamic and acoustic properties of rectangular or high-aspect-ratio nozzles, mostly highlighting their advantages in reducing noise, supporting thrust vectoring, and integrating with aircraft structures in aerospace contexts^{37,38}. However, the absence of detailed turbulence measurements for these configurations presents an obstacle to optimizing nozzle performance for improved efficiency, noise suppression, and pollutant reduction. This study aims to provide detailed measurements of turbulent properties in jets from rectangular nozzles with extended lower lips, particularly assessing radial transport and mixing with ambient air. The present study elucidates the fluid dynamics and time-dependent turbulence of a free jet in a gaseous environment by varying nozzle lip length as a method of flow control.

2. Experimental setup and conditions

132 A schematic illustrating the experimental apparatus and measurement devices is provided in Fig. 1. A
 133 centrifugal blower draws air from an air filter and directs it through a sequence of screens to eliminate any
 134 swirl present in the flow. A rectangular nozzle was mounted on a 200 mm x 200 mm extension section affixed
 135 to the wind tunnel exit. The nozzle has a total length of 190 mm, with 20 mm extending into the extension
 136 section in the x direction, a width, w , of 190 mm in the z direction, and a height (h) of 10 mm in the y direction,
 137 yielding an $AR=19$. The lip length refers to the length of the lower plate extension (L) beyond the end of the
 138 upper plate. The nozzle allows for the replacement of the top and/or bottom plate, enabling the adjustment of
 139 L without modifying the inlet configuration. Measurements were conducted in the xy plane over an axial range
 140 of $0 \leq x/h \leq 30$ and a radial range of $-2.5 \leq y/y_{0.5} \leq 2.5$. Half width, $y_{0.5}$, represents the distance at which the
 141 mean axial velocity reaches half the centreline velocity at the corresponding x/h position. The nozzle centerline
 142 exit velocity, U_o , was maintained at approximately 30 m/s, corresponding to $Re \approx 20100$, with the ambient
 143 temperature held at $19^\circ\text{C} \pm 0.5^\circ\text{C}$.



157 **Fig. 1.** Schematic of the experimental apparatus ① Extension section ② Rectangular nozzle ③ Camera ④ Laser ⑤ hotwire probe
 158 ⑥ 3-D traverse ⑦ Nozzle without plates (half section) ⑧ Equal length nozzle (half section) ⑨ Lip length nozzle (half section).

159 A two-dimensional particle image velocimetry (PIV) system (TSI Incorporated, Minnesota, USA) was
160 employed to visualize the flow. The setup included a double pulse laser (Vlite-200 providing a maximum
161 energy of 200 mJ/pulse, operating at 15 Hz, and delivering a pulse width of 5-8 ns), alongside a charge-coupled
162 device (CMOS) camera (Power View Plus, offering 12 MP resolution of 4096 x 3072 pixels and a frame
163 straddling rate of 180 fps at 10 μ s). The laser and camera were positioned perpendicularly, calibrated spatially,
164 and synchronized via a Laser Pulse Synchronizer (Synchronizer 610036, TSI Incorporated, USA). PIV seeding
165 was introduced at the wind tunnel inlet using a fog generator (developed by Günther Schaidt, SAFEX - Chemie
166 GmbH, Tangstedt, Germany). The time interval Δt was 4 μ s and 10 μ s (for far field and near field) based on
167 the estimated maximum azimuthal velocity (~30 m/s) for no out-of-plane particle and a laser sheet thickness
168 of approximately 1mm. The interrogation window sizes were chosen and set at 64*64 to 32*32 (multi-pass
169 algorithm with 50% overlap) to ensure a maximum of 10 particles per cell by controlling particle density, and
170 a < 25% particle displacement within the cell based on maximum velocity and Δt . Various operational settings
171 were tested and compared to achieve a realistic and correct setup. A spatial calibration was conducted, using
172 the Dantec Dynamics standard 200 mm*200 mm calibration plate. The post-image processing and correction
173 were kept minimal, and the correctness of the images was primarily reliant on the raw captured images. The
174 uncertainty in the PIV measurements is mainly due to the cross-correlation algorithm, with a displacement
175 uncertainty of approximately 0.1 pixel ³⁹. This corresponds to a velocity uncertainty associated with PIV
176 measurements of $\pm 2.015\%$ and $\pm 0.611\%$ in the far field and near field at 30 m/s, respectively, while errors
177 from the scaling factor and the time interval are negligible. Details of the uncertainty calculation are
178 documented in **Supplementary Material #1**.

179 The 2D hot-wire sensor (constant temperature anemometer, 55P61, Dantec, Denmark) featured a diameter of
180 5 μ m and a length of 1.25 mm, with an overheat ratio of 0.8, and was connected to a DANTEC 90N10 hot-
181 wire anemometer system. The hot-wire was calibrated at 15 points, covering a velocity range from 0.5 m/s to
182 35 m/s, using the DANTEC calibration system (Streamline 90H02 Flow Unit) both before and after
183 experimentation. A sampling frequency of 30 kHz was employed, which is adequate to resolve time-averaged
184 turbulent properties of a free jet ⁴⁰, and 200,000 instantaneous data samples were acquired. The probe was
185 mounted on a three-dimensional traversing mechanism (Dantec, Denmark) driven by stepper motors, providing
186 stable and precise sensor positioning. Initially, the centerline velocity at the nozzle exit was established using
187 a pitot tube coupled with a pressure sensor (model: DPBCR0003R-FC, range: 0 ~ 3 kPa, accuracy: $\sim 0.083\%$
188 FS). The velocity outputs from both the pitot tube and the sensor were logged via custom Arduino software.
189 The calibration conducted at the beginning and end of the experiment for both sensors is shown in [Fig.2](#). The
190 resulting curves exhibit nearly perfect overlap, with deviation remaining below 1%, which demonstrates the
191 long-term stability and reliability of the sensors and confirms the absence of significant drift in the hot-wire
192 sensor readings. Therefore, the calibration is applicable throughout the measurement campaign, ensuring
193 accurate velocity data without biases from environmental or sensor changes. The most significant calibration
194 uncertainties measured were 0.4 % at the test's start and 0.6% at the end. The maximum mean error of U was
195 evaluated as $\pm 0.6\%$ on the centerline and $\pm 0.9\%$ in the shear layer, while the uncertainty for second-order
196 velocity fluctuations was determined to be $\pm 4.8\%$ and $\pm 5.2\%$, respectively. All dimensionless and self-

similarity plots were from the comprehensive pointwise velocity data from the CTA measurements. On the other hand, planar measurements were captured using the PIV technique to visualize the entire flow structure.

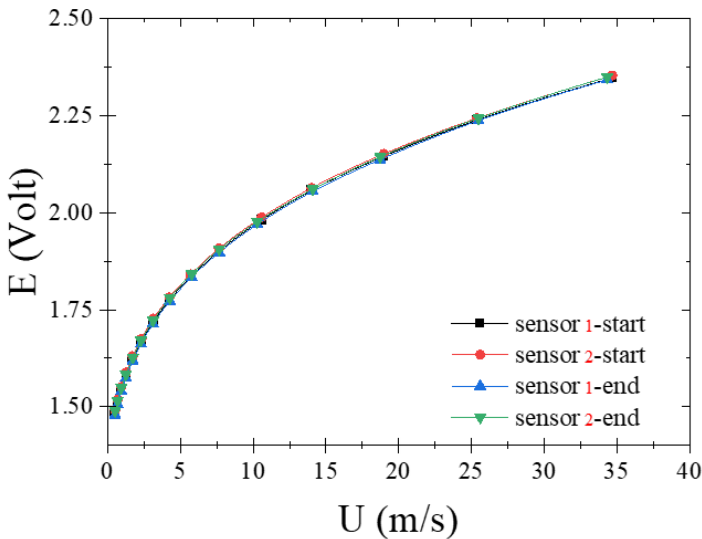


Fig. 2. Calibration curves of the hot wire before and after the experiment.

3. Results and Discussion

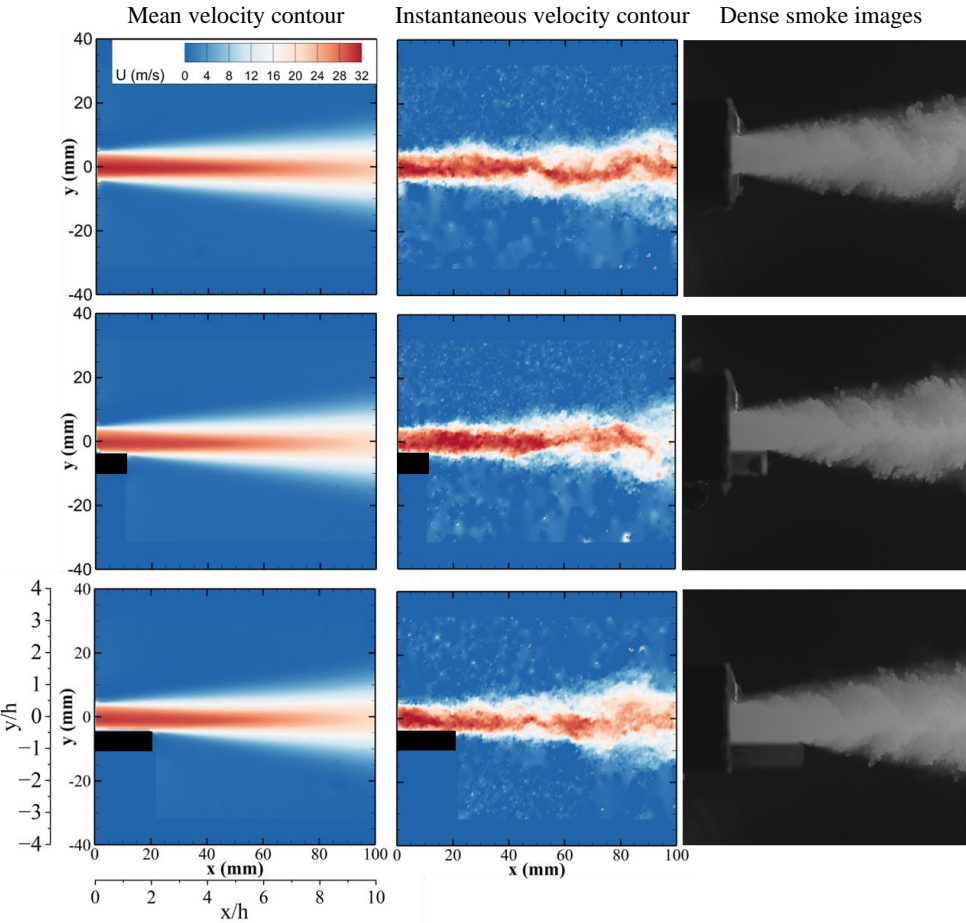
3.1. Velocity fields

3.1.1. Flow visualization

Through the application of Particle Image Velocimetry (PIV) techniques, [Fig. 3](#) illustrates the mean velocity field, instantaneous images, and dense smoke visualizations of the free jet issued from three nozzles with lip lengths of 0mm (L_0), 10mm (L_{10}), and 20mm (L_{20}). Convergence was verified by tracking the mean velocity at representative locations. The velocity stabilized after approximately 300 images, indicating that the results had converged well before reaching the total number of recorded images. Interaction and mixing with the surrounding quiescent air result in immediate momentum redistribution along both the upper and lower edges for the L_0 nozzle, whereas this redistribution occurs later on the lower side as the lip length increases. For the L_0 nozzle, the shear layer encasing the jet core exhibits symmetry. However, for nozzles L_{10} and L_{20} , the shear layer becomes asymmetric, leading to differing upper and lower shear layer characteristics. The high-velocity core diminishes as the axial distance increases, with a more rapid decay in the cases of L_{10} and L_{20} , consequently reducing the potential core region. The increased lip length maintains flow attachment along the surface over an extended region, facilitating greater radial diffusion of the flow on the free side.

3.1.2. Mean axial velocity

The mean axial velocity, normalized by the local centerline axial velocity (U/U_c), is measured along the radial direction, which is normalized by half the velocity profile width ($y/y_{0.5}$), at x/h positions of 0.2, 1, 3, 10, 20, and 30, as shown in [Fig. 4a](#). Additionally, the self-similarity profiles for the three nozzles are provided in [Fig. 4b](#). At $x/h = 0.2$, the velocity profile for the L_0 nozzle exhibits symmetry about the jet center due to the simultaneous interaction and momentum redistribution between the upper (free) and lower (lip) sides of the jet (where positive $y/y_{0.5}$ corresponds to the free side and negative $y/y_{0.5}$ to the lip side) with the surrounding fluid. In contrast, the velocity profiles for the L_{10} and L_{20} nozzles are asymmetric, with the L_{20} nozzle displaying



243 **Fig.3.** PIV visualizations of the free jet in both axial and radial directions for nozzles with varying lip lengths (raw data from PIV).

244 greater asymmetry than the L_{10} . For the L_{20} nozzle, the velocity distribution on the free side is broader and
 245 exhibits increased radial diffusion relative to the L_{10} and L_0 nozzles, whereas the lip side profiles are consistent
 246 across all nozzle types. This difference is attributed to distinct vortex roll-up and momentum transfer
 247 mechanisms between the jet center and edges, which will be elaborated on later. To confirm the agreement
 248 between the two methods, a comparison of CTA and PIV velocity measurements was carried out at multiple
 249 downstream locations (not presented here). The findings confirmed that the average and maximum velocity
 250 deviations between PIV and CTA were 1.4% and 3.6%, respectively.

251 It can be observed that the position of maximum local velocity shifts toward the lip side as the lip length
 252 increases, then returns toward the jet center at a greater downstream location. This pattern is also detected for
 253 $x/h = 1$ and 3, but the effect gradually lessens and becomes negligible at larger downstream distances.

254 Normalized mean axial velocity self-similarity profiles, U/U_c , are presented with the Gaussian, Goertler⁴¹,
 255 Bradbury⁴², and Tollmien⁴³ distributions overlaid to enable direct comparison of the experimental results with
 256 relevant theoretical or empirical models. The degree of self-similarity in turbulent jet velocity profiles depends
 257 on the nozzle configuration—whether axisymmetric or non-axisymmetric—and is further influenced by
 258 geometric modifications to a given nozzle. As the jet progresses downstream, the normalized mean velocity
 259 profiles from each nozzle converge toward a universal distribution. Among the three configurations, at the free
 260 side, the L_{20} nozzle reached self-similarity at a shorter distance, followed by L_{10} and L_0 . The respective axial
 261 positions for achieving self-similarity were $x/h = 1, 3$, and 5 at $y/y_{0.5} \leq 1$. In contrast, for $y/y_{0.5} \geq 1$, the

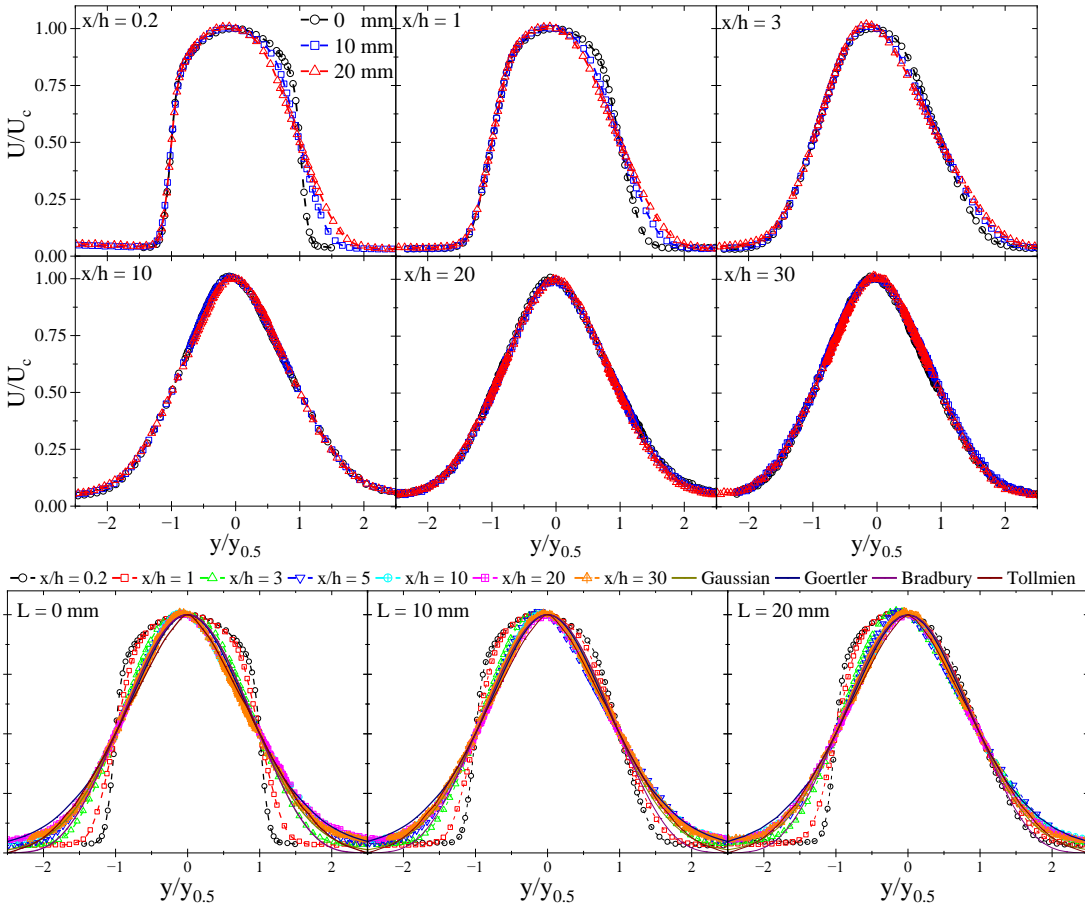


Fig.4. a) Radial profiles of normalized mean axial velocity, U/U_c , b) Self-similarity profiles, in the radial direction, $y/y_{0.5}$, across axial distance for different lip length nozzles (raw data from CTA).

the corresponding x/h values were 3, 5, and 10. The axial distance required for the velocity profile to reach self-similarity varies between the jet core and the peripheral regions, mainly because velocity and turbulence parameters stabilize earlier downstream where geometric effects diminish. However, in the outer region, the influence of ambient fluid entrainment and turbulent dispersion necessitates a longer downstream length for self-similar behavior and for the profiles to align along a universal curve. A comparison of these experimental profiles with the Gaussian distribution reveals good conformity to the classical bell shape, particularly in both the jet center and peripheral zones. Theoretical and empirical/semi-theoretical model predictions show strong agreement with experimental results at $y/y_{0.5} \leq 1$, noting only slight deviations in the outer regions.

The area under each curve, measured up to a cutoff of 0.1 at the peripheral limit, was used to calculate the asymmetric ratio (A_sR) of the velocity profiles as follows:

$$A_sR = \frac{A^+ - A^-}{A^+ + A^-} \quad (1)$$

Where A^+ and A^- represent the areas under the curve on the positive and negative sides of $y/y_{0.5}$, respectively. The asymmetric ratio increases with greater lip length. As axial distance grows, the ratio decreases before exhibiting minor oscillations around 0.5%, as depicted in Fig. 5. At the nozzle exit, the asymmetry percentages for L_0 , L_{10} , and L_{20} were 0.25%, 1%, and 2%, respectively, with a $\pm 0.53\%$ average uncertainty. Details of the uncertainty calculation are documented in **Supplementary Material #2**.

The data show that asymmetry peaks close to the jet exit, followed by a marked decline at $x/h = 3$ and only slight, gradual recovery farther downstream. Additionally, a longer lip length corresponds to greater asymmetry in the near field; however, further downstream, this effect is mitigated by strong turbulent mixing and entrainment.

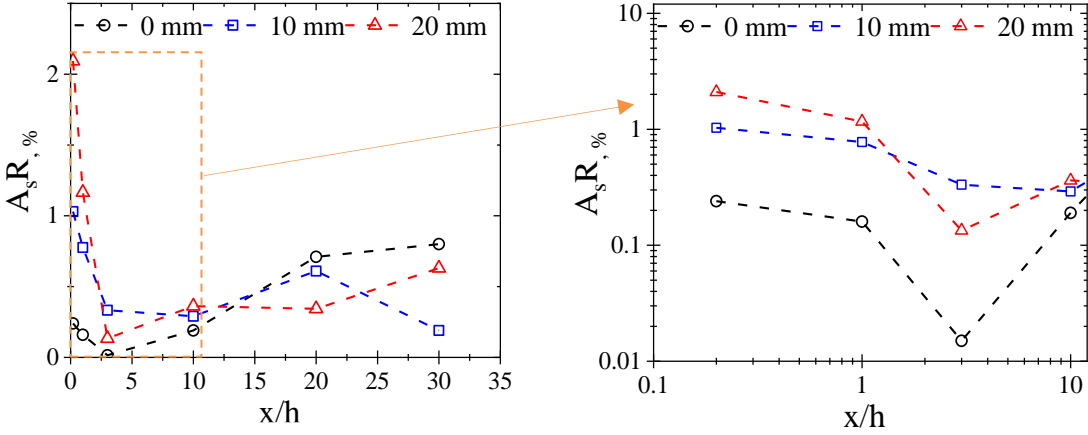
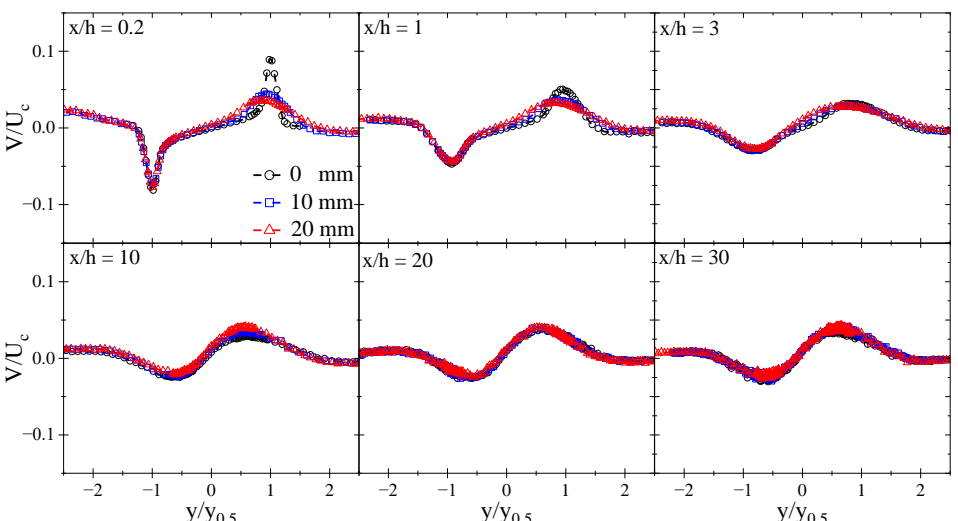


Fig.5. Asymmetric ratio of the normalized axial velocity across axial distance for different lip length nozzles (raw data from CTA).

3.1.3. Mean radial velocity

Normalized radial velocity profiles, V/U_c , at $x/h = 0.2, 1, 3, 10, 20$, and 30 versus $y/y_{0.5}$ are compared with self-similarity profiles in Fig. 6. The initial normalized radial velocity distribution at the nozzle exit ($x/h = 0.2$) demonstrates a sharper radial momentum, exhibiting pronounced peaks at $y/y_{0.5} = \pm 1$ that decay further downstream, along with the peaks shifting radially toward the center and exceeding $y/y_{0.5} = \pm 0.6$ at $x/h=30$. As the axial distance increases, the profiles broaden and their intensity diminishes, before converging into a single self-similar profile. The attenuation of the radial velocity peak can be attributed to the characteristics of free jet nozzles, at which the radial momentum rapidly declines after exiting the nozzle due to air entrainment and flow redistribution, resulting in a relatively smaller radial velocity component compared to the axial component. The effect of the lower lip length extension on the radial velocity of the free side is clearly discernible in the near field, whereas the lip side profile remains nearly unchanged with increasing axial distance. Extended lower lip lengths not only reduce the peak radial velocity, but also broaden its distribution, which enhances the outward momentum and radial spreading on the free side, resulting in a significantly larger radial dispersion area than that observed for the equal-length nozzle. This broadening of the radial velocity profile is particularly significant in industrial applications such as pre-filming air-blast atomizers, where enhanced spray dispersion and spread are advantageous. Experimental findings indicate that both atomizing edge thickness and mean air velocity are key factors affecting not only the disintegration of the liquid film, but also the resulting droplet velocities and trajectories. A broader radial velocity profile permits the atomizing air to interact with the liquid film over a wider region, thereby promoting more effective primary breakup and yielding a more uniform and widely distributed spray.

Rectangular jets serve as a basis for this study due to their application in pre-filming air-blast atomizers, where both nozzle geometry and the air velocity profile at the exit significantly influence breakup duration, atomization quality, and spray distribution, as shown by modelling and experimental studies. The radial extent of the high-speed air region and the associated velocity gradients directly affect the processes leading to



(a)

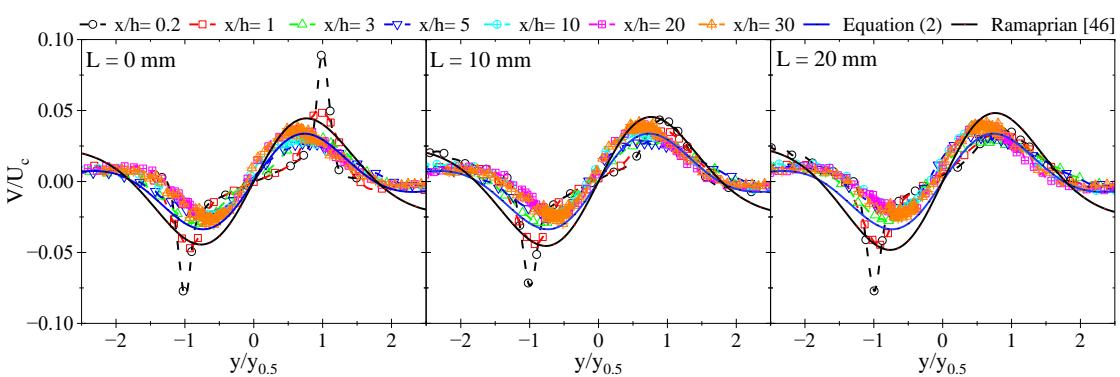


Fig. 6. a) Normalized radial velocity profiles, V/U_c , b) Self-similarity profiles, in the radial direction, $y/y_{0.5}$, across axial distance for different lip length nozzles (raw data from CTA).

primary atomization^{44,45}. The initial disintegration of the liquid is primarily governed by the force applied by high-speed air at the liquid-gas interface. When the axial velocity profile at the exit is elevated, the high-speed air region expands, causing the shear force to be distributed over a broader area of the liquid layer. This enhances the air-liquid interface, leading to more efficient and uniform atomization^{44–46}.

In real-world scenarios, particularly in gas turbine combustors, where optimal atomization is essential for stable and efficient combustion, this effect becomes particularly critical^{46,47}. Simultaneous widening of the axial and radial velocity profiles leads to better mixing, elevated atomization efficiency, and more uniform spray distributions, all of which are vital for the performance of air-blast atomizers in industrial processes such as coating and combustion^{48–51}.

The L_{20} reaches the self-similar region more rapidly than the L_{10} and L_0 , exhibiting profiles in agreement with the trend described by the semi-empirical equation introduced by Ramaprian and Chandrasekhara⁵². Furthermore, the current correlation is capable of approximating the profile using equation (2), where the experimental constants a , b , and c have values of 0.074, -0.024, and 0.53, respectively.

$$\frac{V}{U_c} = \left[a \left(\frac{y}{y_{0.5}} \right) + b \left(\frac{y}{y_{0.5}} \right)^3 \right] \exp(-c \left(\frac{y}{y_{0.5}} \right)^2) \quad (2)$$

Reaching the self-similar region at an earlier stage contributes to superior atomizer performance, finer and more consistent sprays, and superior control and prediction of the atomization process, all of which are essential for achieving high efficiency in combustion and spray systems⁵³⁻⁵⁷.

3.1.4. Mean centerline axial velocity and turbulent intensity

The normalized mean centerline velocity, U_o/U_c , and turbulent intensity, U_{rms}/U_c , are illustrated in Fig. 7. The jet exhibits a sustained potential core region where $U_c \approx 0.98 U_o$, which is followed by a region exhibiting an inverse decay consistent with a 1/2-power law, described by $U_c \sim x^{-1/2}$. For comparison, the data from Suresh et al.¹⁶ ($AR = 20$ and $Re_h = 6250$) are included, showing a trend that aligns closely with the present results. The potential core length, P_c —which is defined as the maximum axial distance where U_c is equal to 0.98 U_o —differs among the nozzle configurations, and is shortest for the L_{20} nozzle. Specifically, the P_c values for the L_0 , L_{10} , and L_{20} nozzles are 3.85h, 2.82h, and 2.37h, respectively. A reduced potential core length reflects an enhanced degree of mixing and flow redistribution, as well as increased air entrainment, which leads to a rise in U_{rms}/U_c for the lip length nozzles, especially with increasing downstream distance⁵⁸⁻⁶⁰.

Since the jet's momentum and energy dissipate and mix into the ambient air more effectively and rapidly in lip length nozzles, the RMS of velocity fluctuations decreases more sharply for these cases. Notably, sharp peaks in U_{rms} that typically elevate noise and diminish mixing uniformity^{61,62} were not observed in the present data. As the flow progresses further downstream, asymptotic values near 0.2 are attained, which is consistent with what has been previously reported⁶³.

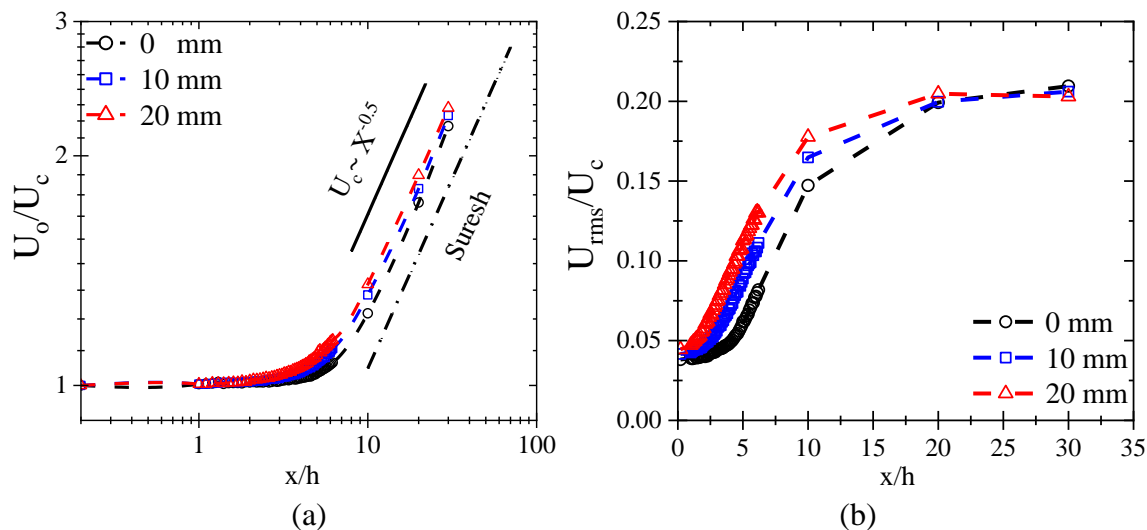
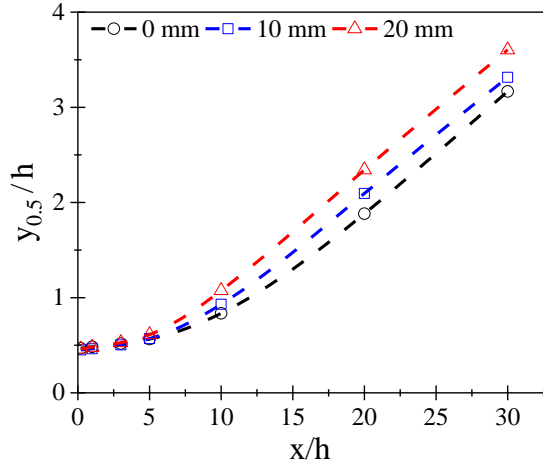


Fig. 7. a) Variation of normalized centerline mean axial velocity, U_o/U_c , compared to data from Suresh et al., b) the normalized centerline turbulence intensity, across axial distances (raw data from CTA).

3.1.5. Jet half widths

Figure 8 presents the variation in the jet's half-width for different lip length nozzles along the axial direction at the free side, revealing a consistently increasing trend downstream. For $x/h \geq 10$, the established correlation $y_{0.5}/h = SR_y(x/h + V_{or}/h)$ ^{16,63} fits the half-width measurements well, providing spreading rate (SR_y) values of 0.1166, 0.1192, and 0.1265 for L_0 , L_{10} , and L_{20} , respectively. As the spreading rate increases, the virtual origin (V_{or}) shifts closer to the nozzle exit; the corresponding V_{or}/h values are -3.17, -2.27, and -1.49 for L_0 , L_{10} , and

394 L_{20} , respectively. The L_{20} nozzle demonstrates a shorter potential core, reduced centerline velocity, and higher
 395 U_{rms} , all of which indicate enhanced air entrainment and penetration into the jet, leading to an elevated
 396 spreading rate. On the other hand, L_0 shows the weakest spreading behavior, signifying that the flow stays
 397 more confined with an extended potential core region.

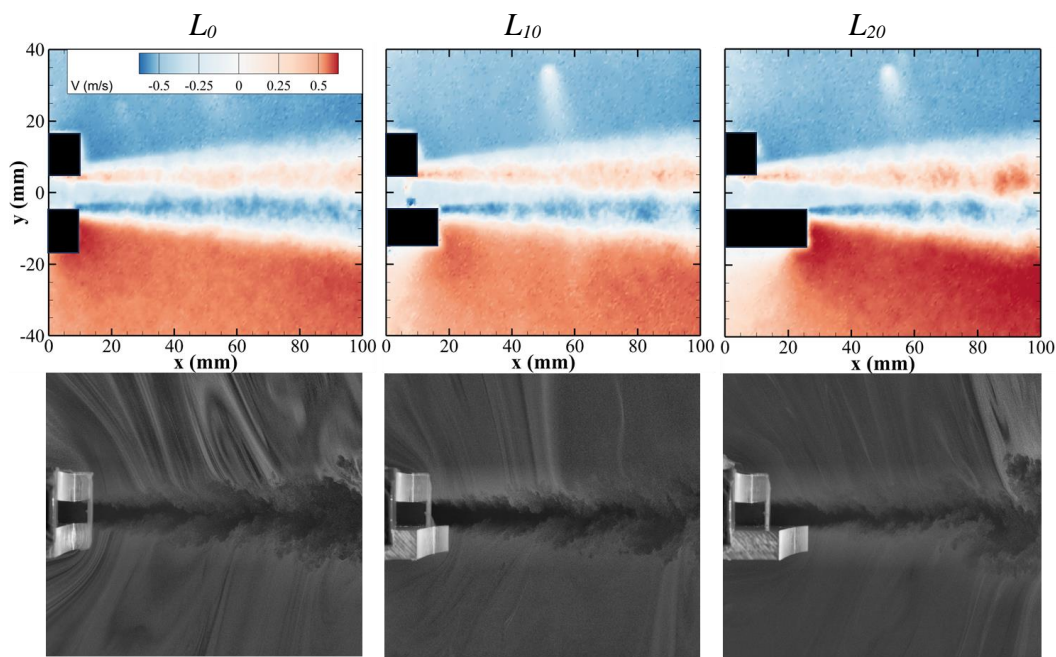


405 **Fig. 8.** Free side half width dependency on the nozzle lip length across axial distance (raw data from CTA).

406 **3.2. Air entrainment**

407 **3.2.1. Flow visualization**

408 A qualitative assessment of air entrainment and the radial motion of the flow is depicted in Fig. 9. It is apparent
 409 that the jet propagates and spreads outward as previously described, with this process driven by momentum
 410 redistribution, mixing, and air entrainment from the surrounding quiescent air. Near the jet boundary, the
 411 entrained air moves toward the jet core on both sides, illustrating how ambient air is drawn into the jet.
 412 Additionally, for the L_0 nozzle, interaction with the surroundings initiates simultaneously on both sides; for
 413 the L_{10} and L_{20} nozzles, the onset on the lip side occurs later.



424 **Fig. 9.** Qualitative visualization of air entrainment for different lip length nozzles; 1) Radial velocity, 2) Dense smoke images (raw
 425 data from PIV).

425 **3.2.2. Nondimensional volume flow rate**

426 At any axial location x from the nozzle, the volume flow rate for a rectangular nozzle can be determined
 427 through an area integral of the axial component of the mean velocity:

428

$$Q = w \int_0^{\infty} U(y) dy \quad (3)$$

429 The area beneath the curve was computed using a combination of Simpson's and trapezoidal integration
 430 methods. To ensure a fair comparison among the nozzles, the integration domain is restricted to the radial
 431 position at which the axial velocity reaches 10% of the centerline velocity ⁶⁴.

432 Upon normalization by the centerline velocity and the half-width, the following relationship is obtained:

433

$$Q = w U_c y_{0.5} \int_0^{y_{0.1}} U^*(y^*) dy^* \quad (4) \quad \text{where, } U^* = \frac{U}{U_c}, y^* = \frac{y}{y_{0.5}}$$

434 Consequently, the nondimensional volume flow rate is:

435

$$Q^* = \int_0^{y_{0.1}} U^*(y^*) dy^* \quad (5)$$

436 The ratio of the nondimensional volume flow rate at any given axial position, Q_x^* ($Q_x^* = Q_x^* + Q_e^*$) to that at
 437 the exit, Q_0^* , is shown in Fig. 10. The extent of air entrainment increases with greater lip length, attributed to
 438 earlier vortex formation and enhanced interaction with the surroundings, which propels air into the jet. There
 439 is a 4% and 2% rise in air entrainment for the L_{20} and L_{10} nozzles, respectively, relative to the L_0 nozzle at the
 440 exit.

441 Nozzles with extended lip lengths exhibit higher air entrainment compared to their equal-length counterparts
 442 up to $x/h = 10$. Beyond this point, the free jet's entrainment behavior becomes independent of the initial nozzle
 443 geometry, although unique characteristics are retained due to the turbulence's dynamics and vortex shedding.
 444 Once the flow reaches fully developed turbulence, jet mixing and air entrainment follow general trends
 445 governed by turbulent jet dynamics ⁶⁵.

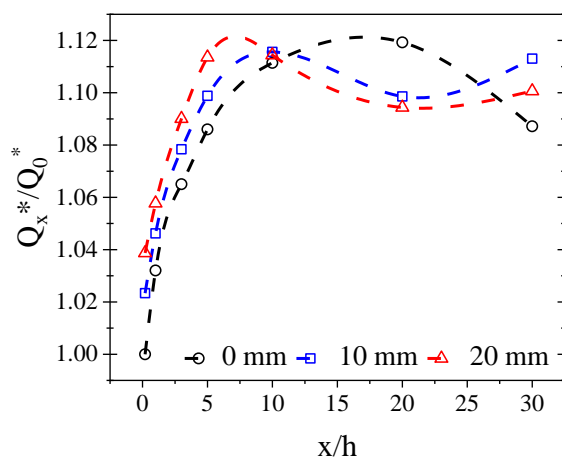


Fig. 10. Normalized nondimensional volume flow rate as a function of axial distance for different nozzle lip lengths (raw data from CTA).

453 **3.3. Turbulent characteristics**

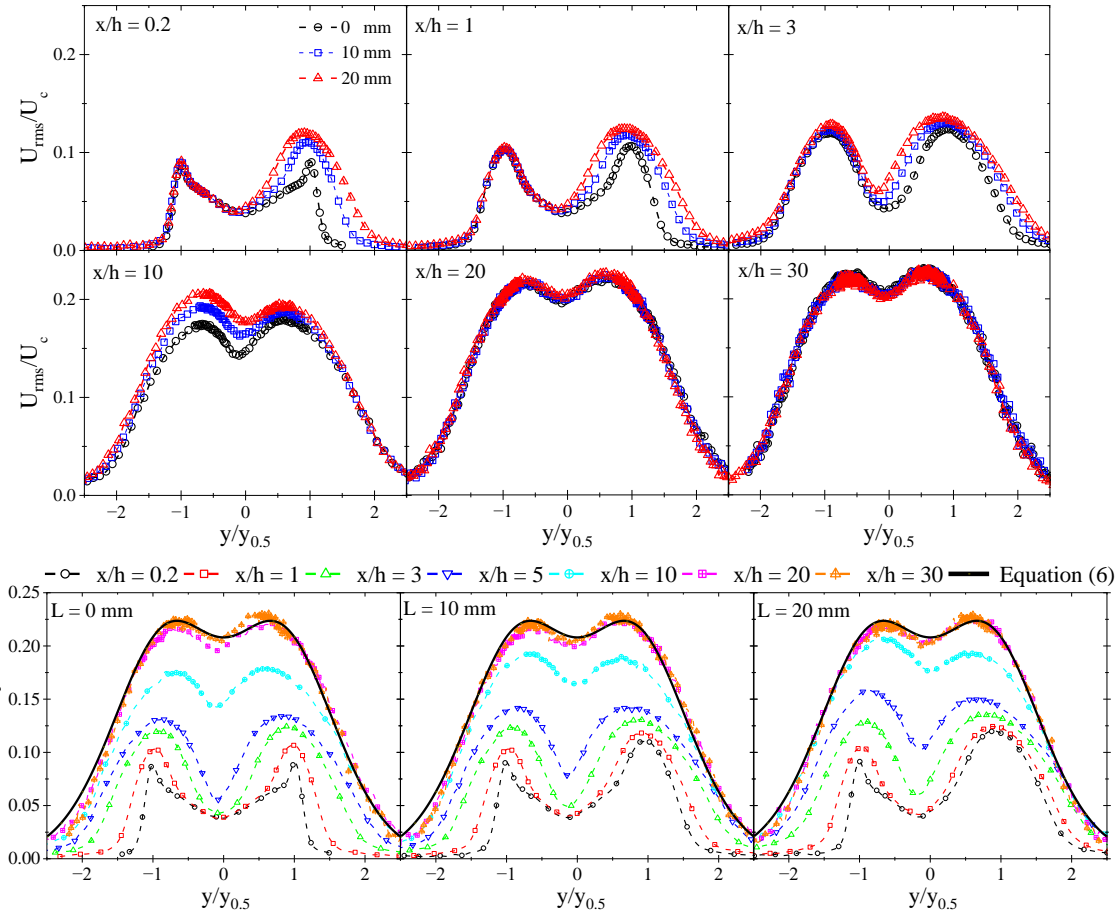
454 **3.3.1. Turbulent intensity distributions of the axial velocity**

455 Figure 11 displays the radial variation of the normalized root mean square of axial velocity fluctuations,
 456 U_{rms}/U_c , and demonstrates the attainment of self-similarity with increasing axial position. In all cases, two
 457 separate peaks are evident, reflecting the existence of a dual shear layer structure; nonetheless, both the
 458 magnitude and shape of these peaks are influenced by the lip length. The results indicate that, in the near field,
 459 peak intensities and widths increase on the free side with longer lip lengths, and this pattern persists with
 460 increasing axial position until the peak magnitudes stabilize. These observations suggest that increasing the lip
 461 length enhances turbulence and velocity fluctuations in the free side, which is primarily caused by increased
 462 air entrainment and asymmetries generated by the nozzle lip design.

463 The centerline value and the values at the two peaks increase with downstream distance and with increasing
 464 lip length, ultimately reaching an asymptotic value of approximately 0.25^{16,66}. The profiles attain self-
 465 similarity more quickly as the centerline and peak values rise for the lip length nozzles, while maintaining the
 466 two peaks even at $x/h = 30$. Furthermore, the data closely fit the empirical equation (6), which represents a
 467 modification of the formulation proposed by Miller and Comings⁶⁷.

$$468 \frac{U_{rms}}{U_c} = a \exp(-b (\frac{y}{y_{0.5}})^2) - c \exp(-d (\frac{y}{y_{0.5}})^2) \quad (6)$$

469 Here, a, b, c, and d denote experimental constants with values of 0.509, 0.51, 0.301, and 1.13, respectively.



483 **Fig. 11.** a) Variation of normalized root mean square (rms) of the axial velocity fluctuations, U_{rms}/U_c , in the radial direction, $y/y_{0.5}$, b) Self-similarity profiles across axial distance for different lip length nozzles (raw data from CTA).

3.3.2. Distributions of the turbulent intensity for the radial velocity

The variation in normalized root mean square (rms) values of the radial velocity, V_{rms}/U_c , and the associated self-similarity profiles are presented in Fig.12. The general trend of these profiles aligns with that of U_{rms}/U_c for $x/h \leq 3$, but downstream the profile transitions to a single peak with a value near 0.18. Close to the nozzle exit, intense shear layers at the jet boundaries induce strong turbulence, producing two distinct peaks in the velocity fluctuation profile; nonetheless, the shear layer on the free side broadens, and centerline values increase with greater lip length before stabilizing. With downstream distance, turbulent mixing and momentum diffusion facilitate peak merging and broadening, resulting in a more symmetric, single-peaked profile that indicates the establishment of a self-similar turbulent jet structure in terms of cross-stream fluctuations. At higher x/h values, the normalized profiles converge onto a universal curve, highlighting self-similar behavior irrespective of initial jet conditions, and can be described by equation (6), substituting U_{rms} with V_{rms} and adopting 0.205, 0.4, 0.023, and 1.9 as the constants a , b , c , and d , respectively. As turbulent transport and mixing progressively surpass the influence of the original jet characteristics, the turbulent jet reaches a universal profile of normalized velocity fluctuations at sufficiently large downstream distances, independent of the initial setup. The appearance of two peaks in U_{rms}/U_c can be attributed to vortex shedding phenomena, where axial velocity fluctuations are most pronounced within the alternating shear layers due to vortex formation and detachment. Conversely, a single peak in V_{rms}/U_c is observed because the cross-stream fluctuation profiles from both shear layers overlap at the centerline as vortices interact and merge further downstream^{68,69}, a mechanism further elaborated in the discussion on turbulent transport products.

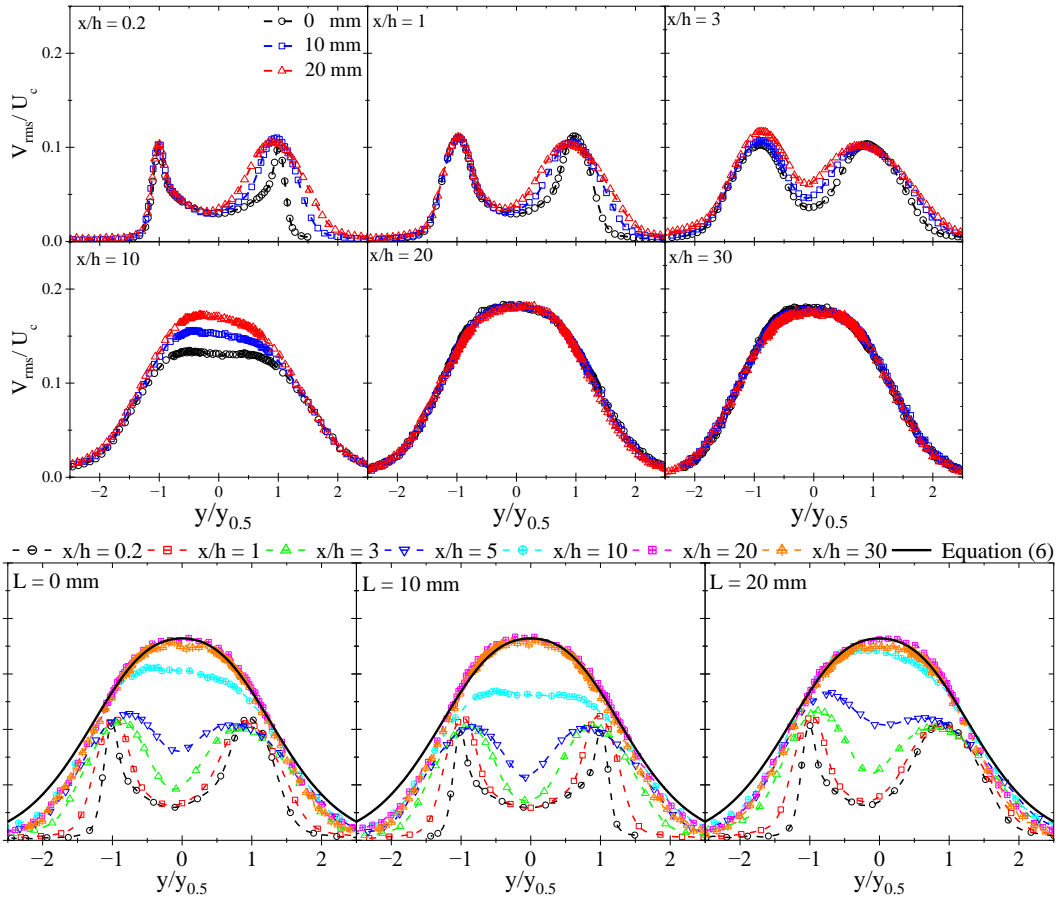
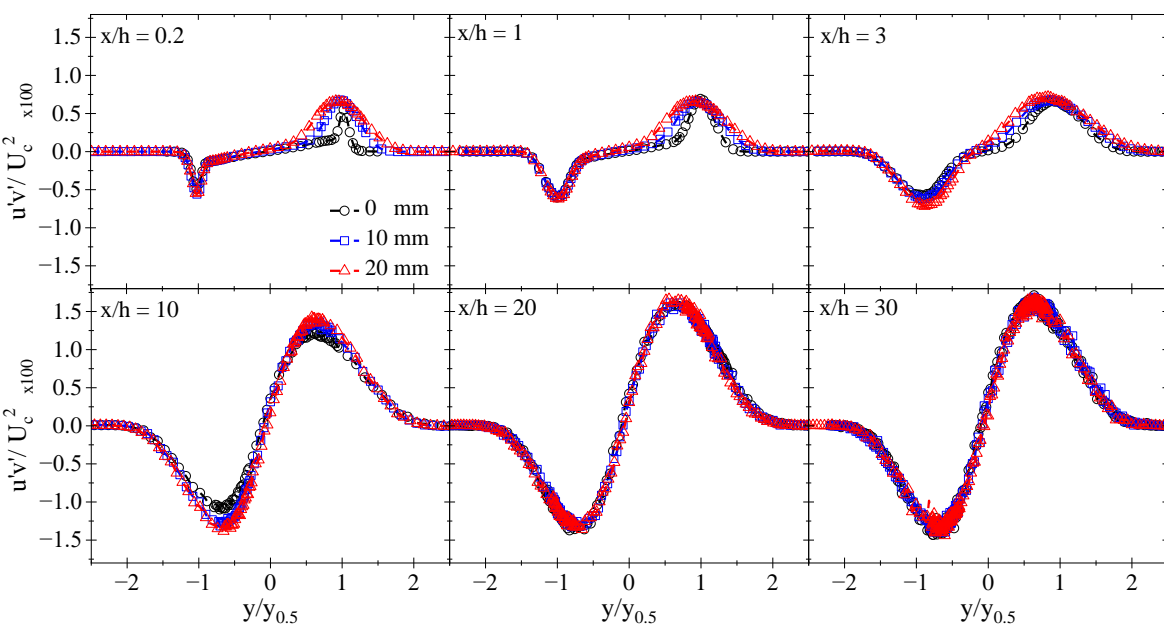


Fig. 12. a) Variation of normalized root mean square (rms) of the radial velocity fluctuations, V_{rms}/U_c , in the radial direction, $y/y_{0.5}$, b) Self-similarity profiles, across axial distance for different lip length nozzles (raw data from CTA).

516 **3.3.3. Shear stress and triple velocity product**

517 The normalized shear stress at various downstream positions is presented in Fig.13. The largest Reynolds shear
 518 stresses are observed in the shear layers, where turbulence generation and significant large-scale vortex motion
 519 take place ^{15,70}. Analysis of the RMS distributions of the velocity components indicates that the shear stress
 520 peaks are located near $y/y_{0.5} = \pm 1$ at the nozzle exit, with these peaks gradually shifting toward the jet center
 521 as the axial distance increases ¹⁵. The maximum values of shear stress on the lip side remain approximately
 522 constant, while on the free side, the profiles are notably broader for the lip length nozzles, indicating enhanced
 523 turbulence and a more robust momentum transfer region within the jet. A wider shear stress profile on the free
 524 side suggests an expanded mixing region, contributing to a more uniform distribution of energy and momentum
 525 within the jet ⁷¹. At greater axial distances, the shear stress increases as a result of amplified axial and cross-
 526 stream velocity fluctuations and the profiles approach a self-similar pattern ⁷².

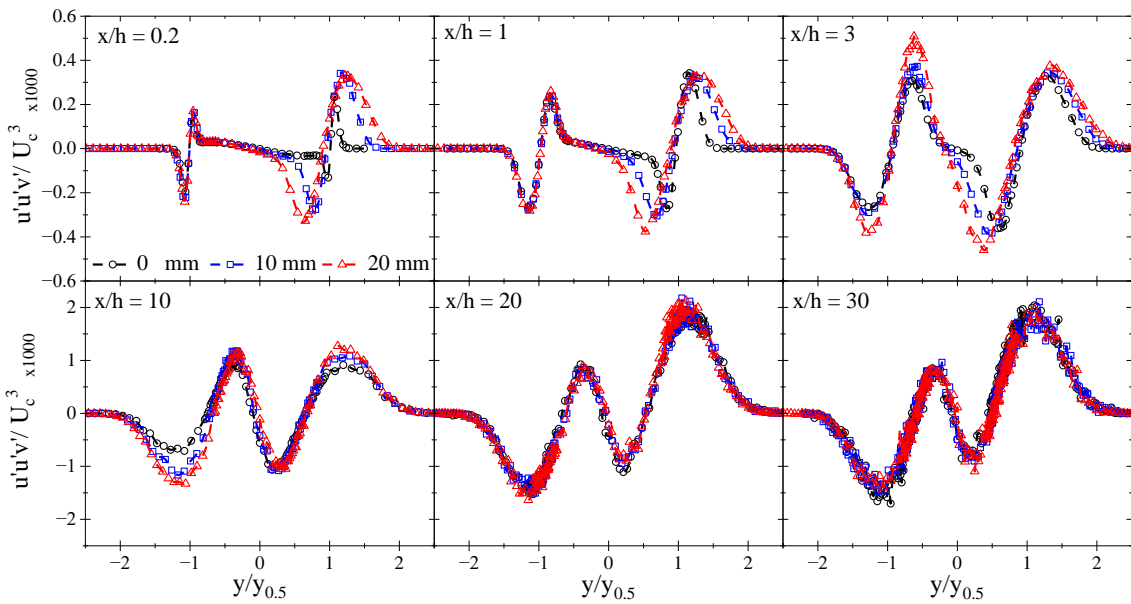


537 **Fig. 13.** Variation of normalized shear stress, uv'/U_c^2 , in the radial direction, $y/y_{0.5}$, across axial distance for different lip length
 538 nozzles (raw data from CTA).

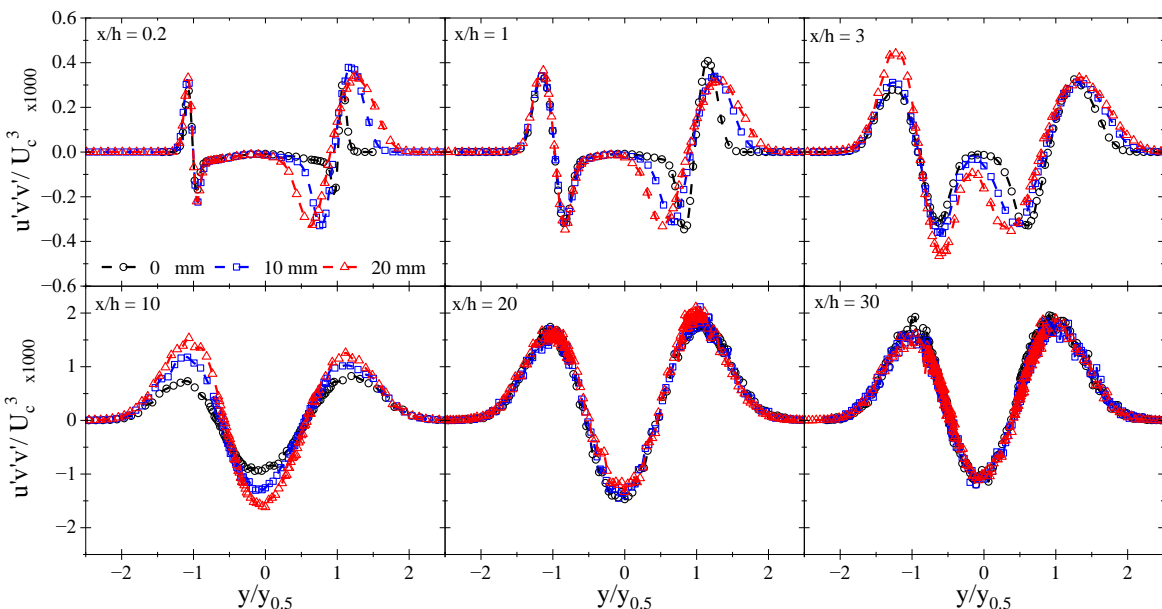
539 The profiles of the normalized third-order moment of velocity fluctuations in Fig.14 and Fig.15 depict the
 540 turbulent transport of Reynolds normal stress (axial turbulent kinetic energy $u'u'$) and Reynolds shear stress
 541 (uv') facilitated by the cross-stream velocity fluctuation (v'), which plays a key role in the momentum transport
 542 and mixing layer formation within the jet ^{15,25}.

543 The interaction of the air jet with the surrounding quiescent air induces the formation of vortices in the shear
 544 layer by Kelvin–Helmholtz instability ⁷³ and air entrainment. The nearly flat, zero value observed at the center
 545 region indicates the potential core zone where the velocity remains constant. As the flow progresses
 546 downstream, entrained air penetrates the jet, and once the core and vortices break down, velocity fluctuations
 547 and turbulent transport increase, leading to more intense mixing and enhanced turbulence. On one side of the
 548 vortices, they move air inward towards the jet core, while on the opposite side, they transport air outward from
 549 the jet core to the boundary. As a result, significant fluctuations and turbulent transport occur at the interfaces,

550 promoting mixing and redistribution of momentum ⁷⁴ and resulting in a more radially dispersed flow pattern
 551 for the lip length nozzles. The results indicate that turbulent transport is directed toward the centerline for $-1 \leq y/y_{0.5} < 1$, while at $1 \leq y/y_{0.5} < -1$, the direction shifts toward the outer edges, with zero values at the
 552 extremities ^{17,65}. The L_{20} nozzle produces larger inward and outward turbulent transport regions across the
 553 layers compared to the L_{10} and L_0 nozzles, resulting in increased centerline velocity decay, greater jet spread,
 554 and enhanced centerline turbulence.
 555



556
 557
 558
 559
 560
 561
 562
 563
 564
Fig. 14. Variation of turbulent transport of Reynolds normal stress ($u' u'$) by the cross-stream velocity fluctuation (v'),
 565 $u' u' v' / U_c^3$, in the radial direction, $y/y_{0.5}$, across axial distance for different lip length nozzles (raw data from CTA).



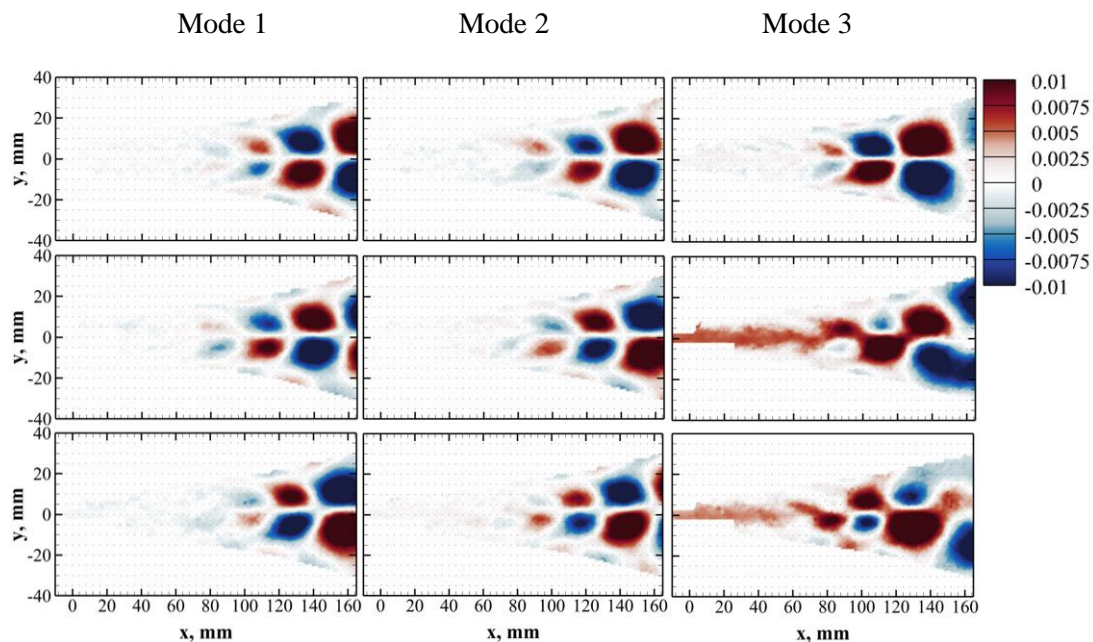
567
 568
 569
 570
 571
 572
 573
Fig. 15. Variation in the turbulent transport of Reynolds shear stress ($u' v'$) caused by cross-stream velocity fluctuations (v'),
 574 $u' v' v' / U_c^3$, measured in the radial direction, $y/y_{0.5}$, across the axial distance for different nozzle lip lengths (raw data from CTA).

576 **3.4 Coherent structures**

577 The flow's coherent structures, with respect to the effect of lip length, were analyzed using classic Proper
 578 Orthogonal Decomposition (POD) based on 4000 snapshots obtained through the snapshot method, the details
 579 of which are well documented in the literature ⁷⁵. Upon evaluation of the turbulent flow field via POD, it was
 580 observed that primary flow features were less dominant than expected, as turbulent kinetic energy was
 581 distributed across many modes. This observation is in agreement with the inherent limitations of POD ⁷⁶. While
 582 the turbulent kinetic energy associated with the leading POD modes was relatively low (with the energy of the
 583 first mode at 3%) for all three nozzles, suggesting a fully turbulent and complex jet behavior, a comparative
 584 assessment of each mode's spatial structure revealed significant differences likely arising from variations in
 585 nozzle geometry.

586 **3.4.1 POD of axial velocity**

587 Distinct spatial flow patterns for the three nozzle configurations are shown in Fig. 16. Importantly, the initial
 588 modes indicate that the coherent structure persists but with a phase shift. The recurrence of large-scale vortices
 589 can be attributed to similarities in the mode structures, which maintain coherence with a consistent phase delay.
 590 In the higher modes, where less energy is present, both the scale and rotational orientation of these large
 591 vortical structures become increasingly asymmetric for the lip length nozzle. Mode 3 demonstrates that
 592 changes in nozzle geometry can influence the formation of coherent patterns within jet flows, thereby
 593 impacting downstream turbulence and enhancing mixing by promoting the alternating shedding of both small
 594 and large structures at the jet core and periphery.



603 **Fig. 16.** Full field POD modes for different lip length nozzles (raw data from PIV).

604 The POD analysis over the full field-of-view showed no discernible structures near the nozzle exit ($x < 70$
 605 mm), as the energy associated with these structures was significantly lower relative to downstream features.
 606 To identify any such near-field structures, the corresponding POD analysis is shown in Fig. 17.

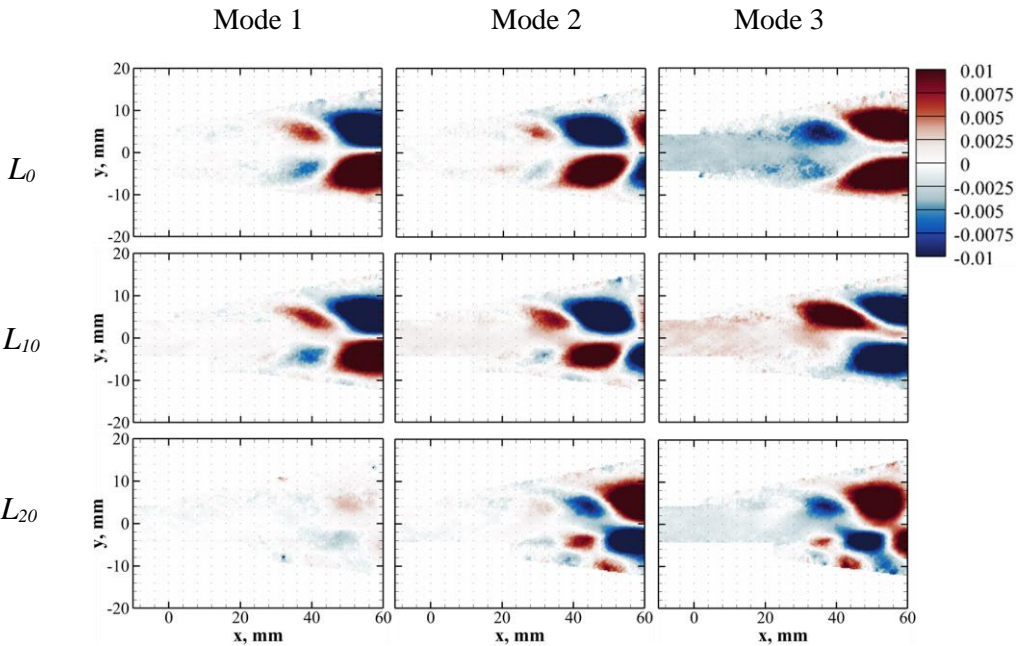


Fig. 17. Near field POD modes for different lip length nozzles (raw data from PIV).

Similar to the full POD field, the near-field analysis of the axial velocity reveals pronounced asymmetry, characterized by both small and large stretched structures as the lip length increases. In the full and near-field analyses, as large coherent structures break down into smaller ones, the flow exhibits increased disorder and is dominated by finer, less organized turbulent motions. This indicates a redistribution of energy from large-scale coherent structures to finer-scale turbulent fluctuations through the turbulence cascade, leading to enhanced turbulent mixing and greater overall turbulence intensity^{77,78}.

3.4.2 Structure around the jet

As previously discussed, the interaction between the jet and the surrounding stagnant air begins immediately as the jet exits the nozzle, though the interaction along the lip side is delayed. The Gamma criterion was employed and shown in Fig. 18 alongside the velocity vectors to identify vortices, instabilities, and mixing within the air jet shear layer. The velocity vectors demonstrate entrainment of airflow from outside the shear

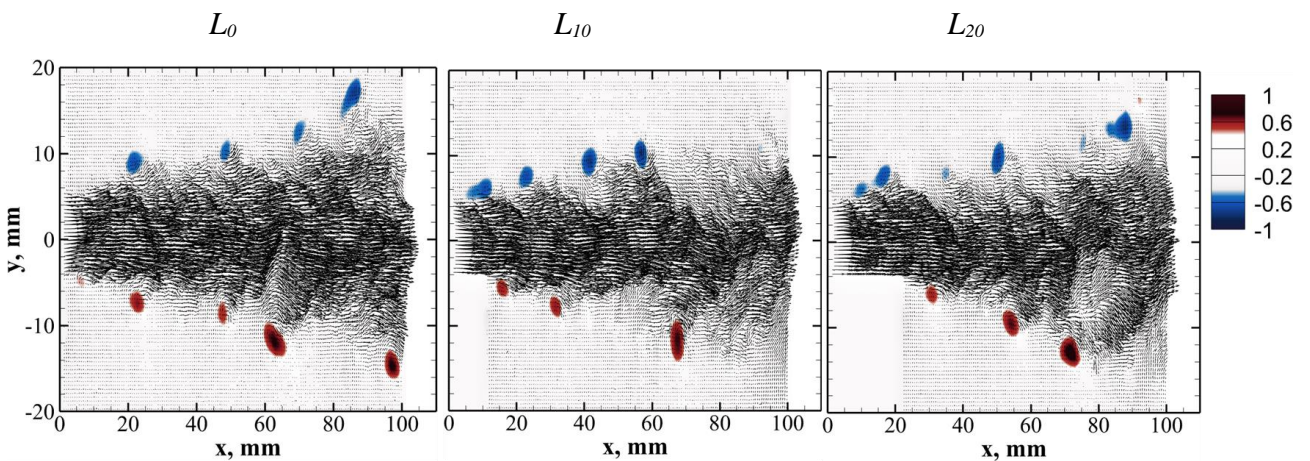


Fig. 18. Instantaneous Gamma criterion analysis for different lip length nozzles (raw data from PIV).

layer into the jet, accompanied by vortex roll-up. The L_{10} and L_{20} nozzles display asymmetry in the vortex roll-up, in contrast to the relatively symmetric vortex roll-up for the L_0 nozzle, validating the delayed interaction associated with increased lip length.

To further explore the vortex formation in the shear layer, a POD evaluation using the Gamma criterion is illustrated in Fig. 19. The leftmost column displays the time-averaged flow field, which highlights the delayed interaction with the surrounding air as the lip length increases. Modes 1 to 3 depict the spatial development of key coherent structures. The spatial arrangement and intensity of these structures vary with increasing lower lip length. In the shear layer around the jet for the L_0 nozzle, both the mean flow and modes appear symmetric. As lip length increases, the asymmetry in both the mean flow and corresponding modes becomes more pronounced, verifying alterations in the jet's shear layer dynamics and its interaction with the ambient air.

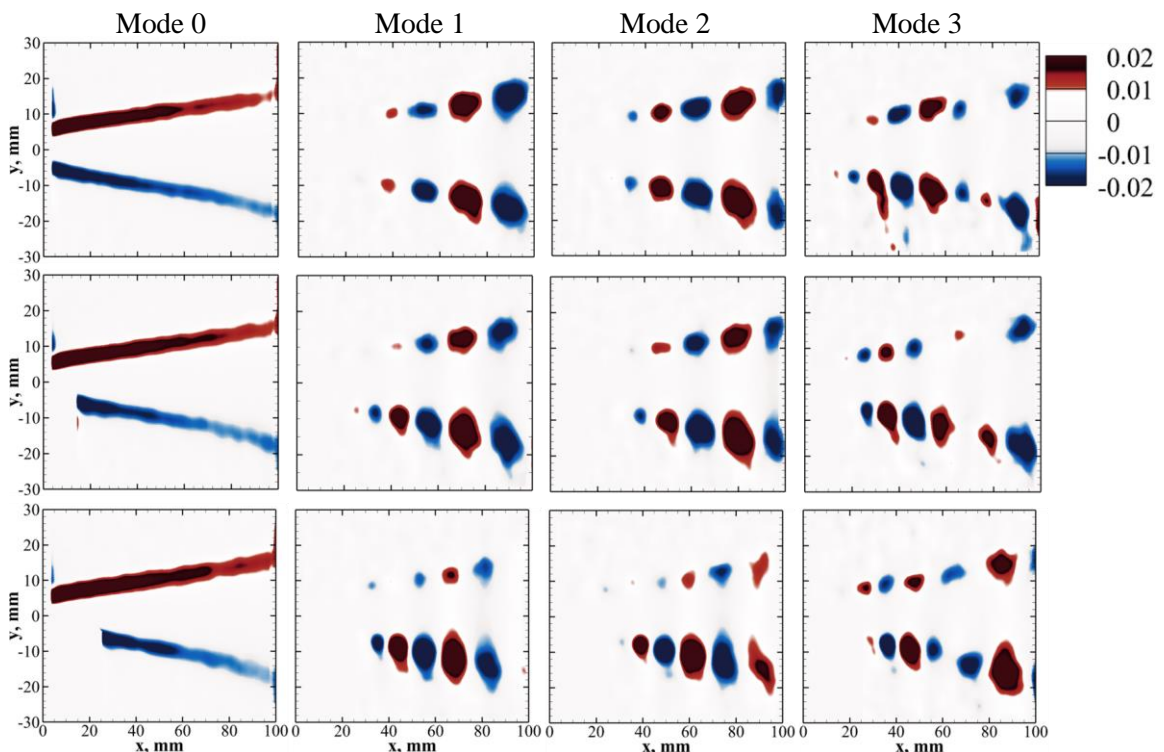


Fig. 19. POD modes of the Gamma criterion for various lip length nozzles (raw data from PIV).

4. Conclusions

The effects of lip length extension in a rectangular nozzle with an aspect ratio of 19 on both mean and turbulent flow characteristics were examined experimentally. The findings indicate that increasing the lip length induces asymmetry between the upper and lower shear layers compared to the equal-length nozzle, leading to variations in spreading rate and air entrainment. Nozzles with extended lip length display a greater normalized mean axial velocity in the radial direction, with a displacement of the maximum velocity location. With increased lip length, the maximum radial velocity declines and the flow demonstrates a wider and more pronounced radial movement on the free side. Across all mean and turbulent characteristics, the similarity profiles downstream converge onto a universal curve that is independent of exit geometry, which is consistent with established

theoretical and empirical models. Changes in air intrusion and mixing with the jet periphery and core decrease the potential core length and enhance turbulence along the centerline, which leads to an increased jet half-width and elevated volume flow rate in lip-length nozzles. Additionally, farther downstream, the axial turbulence intensity rises and broadens as lip length increases. The radial turbulence intensity has a slightly lower peak and more spread-out profile at the free side when the lip length is increased, before recovering and rising further downstream. Trends for shear stress, the turbulent transport of Reynolds normal stress, and the turbulent transport of Reynolds shear stress by radial velocity fluctuations consistently became broader and increased with longer lip lengths. POD analysis for the axial velocity and gamma criterion demonstrated the effect of nozzle lip length in producing asymmetric flow structures.

Supplementary Material

See the supplementary materials for a detailed partial-derivative derivation and calculation of the uncertainties in the PIV measurement, including its sources, and in the asymmetric ratio.

Credit authorship contribution statement

Youssef Gamal Nasr Ahmed: Software, Validation, Formal analysis, Writing – original draft, Visualization, Investigation. **Reza Alidoost Dafsari:** Validation, Formal analysis, Writing - review & editing, Visualization, Investigation. **Jeekeun Lee:** Conceptualization, Supervision, Writing – review & editing.

Declaration of Competing Interest

The authors declare that they have no known competing financial interests or personal relationships that could have appeared to influence the work reported in this paper.

Data availability

Data will be made available on request.

References

- ¹ J. Tian, Free Surface Confinement Effects on a Round Jet, *Scholarship at UWindsor*, (2010). <https://hdl.handle.net/20.500.14776/1763>
- ² E. Morris, *Experimental Investigation of Twin and Triple Elliptic Free Jets with Various Nozzle Orientations*, *M.Sc. thesis, University of Manitoba, Winnipeg, Canada*, (2020). <http://hdl.handle.net/1993/34728>
- ³ S.B. Pope, *Turbulent Flows* (Cambridge University Press, Cambridge, 2000). <https://doi.org/10.1017/CBO9780511840531>
- ⁴ C.G. Ball, H. Fellouah, and A. Pollard, “The flow field in turbulent round free jets,” *Progress in Aerospace Sciences* **50**, 1-26 (2012). <https://doi.org/10.1016/j.paerosci.2011.10.002>
- ⁵ C.O. Iyogun, and M. Birouk, “Effect of sudden expansion on entrainment and spreading rates of a jet issuing from asymmetric nozzles,” *Flow, Turbulence and Combustion* **82**(3), 287-315, (2009). <https://doi.org/10.1007/s10494-008-9176-9>
- ⁶ Aleyasin, N. Fathi, M.F. Tachie, and M. Koupriyanov, “Comparison of turbulent jets issuing from various sharp contoured nozzles,” in *American Society of Mechanical Engineers, Fluids Engineering Division, FEDSM*, (2017). <https://doi.org/10.1115/FEDSM2017-69419>
- ⁷ D. Menon, V. Sanjay Shivam, V. TU, A.B. Raikar, and N. Baranwal, “Performance comparison of rectangular nozzle with circular nozzle of military aircraft engine,” in *Materials Today Proceedings* **72**(3), 626-630 (2023). <https://doi.org/10.1016/j.matpr.2022.08.231>

- ⁸ K. Viswanath, R. Johnson, A. Corrigan, K. Kailasanath, P. Mora, F. Baier, and E. Gutmark, "Noise characteristics of a rectangular vs circular nozzle for ideally expanded jet flow," in *54th AIAA Aerospace Sciences Meeting*, (2016). <https://doi.org/10.2514/6.2016-1638>
- ⁹ K.B.M.Q. Zaman, "Axis switching and spreading of an asymmetric jet: The role of coherent structure dynamics," *Journal of Fluid Mechanics* **316**, 1-27, (1996). DOI: <https://doi.org/10.1017/S0022112096000420>
- ¹⁰ M. Xu, A. Pollard, J. Mi, F. Secretain, and H. Sadeghi, "Effects of Reynolds number on some properties of a turbulent jet from a long square pipe," *Physics of Fluids* **25**(3), 035102 (2013). <https://doi.org/10.1063/1.4797456>
- ¹¹ A. Ghasemi, V. Roussinova, R. Balachandar, and R.M. Barron, "Reynolds number effects in the near-field of a turbulent square jet," *Experimental Thermal and Fluid Science* **61**(C), 249-258, (2015). <https://doi.org/10.1016/j.expthermflusci.2014.10.025>
- ¹² T. J. Tipnis, "Effects of Upstream Nozzle Geometry on Rectangular Free Jets," *Ph.D. thesis, Cranfield University, Cranfield Defence and Security*, (2009). <http://ethos.bl.uk/OrderDetails.do?uin=uk.bl.ethos.520385>
- ¹³ J. Mi, R.C. Deo, and G.J. Nathan, "Characterization of turbulent jets from high-aspect-ratio rectangular nozzles," *Physics of Fluids* **17**(6), 068102 (2005). <https://doi.org/10.1063/1.1928667>
- ¹⁴ R.C. Deo, G.J. Nathan, and J. Mi, "Comparison of turbulent jets issuing from rectangular nozzles with and without sidewalls," *Experimental Thermal and Fluid Science* **32**(2), 596-606, (2007). <https://doi.org/10.1016/j.expthermflusci.2007.06.009>
- ¹⁵ M. Alnahhal, and T. Panidis, "The effect of sidewalls on rectangular jets," *Experimental Thermal and Fluid Science* **33**(5), 838-851, (2009). <https://doi.org/10.1016/j.expthermflusci.2009.03.001>
- ¹⁶ P.R. Suresh, K. Srinivasan, T. Sundararajan, and S.K. Das, "Reynolds number dependence of plane jet development in the transitional regime," in *Physics of Fluids* **20**(4), 044105 (2008). <https://doi.org/10.1063/1.2904994>
- ¹⁷ P.M. Sforza, M.H. Steiger, and N. Trentacoste, "Studies on three-dimensional viscous jets," *AIAA Journal* **4**(5), (1966). <https://doi.org/10.2514/3.3549>
- ¹⁸ N. Trentacoste, and P. Sforza, "Further experimental results for three- dimensional free jets," *AIAA Journal* **5**(5), (1967). <https://doi.org/10.2514/3.4096>
- ¹⁹ A. Krothapalli, D. Baganoff, and K. Karamcheti, "On the mixing of a rectangular jet," *Journal of Fluid Mechanics* **107**, 201-220, (1981). <https://doi.org/10.1017/S0022112081001730>
- ²⁰ P.M. Sforza and W. Stasi, "Heated three-dimensional turbulent jets," *Journal of Heat Transfer* **101**, 353–360 (1979). <https://doi.org/10.1115/1.3450973>
- ²¹ A.A. Sfeir, "Investigation of three-dimensional turbulent rectangular jets," *AIAA Journal* **17**(10), (1979). <https://doi.org/10.2514/3.61277>
- ²² A.A. Sfeir, "The velocity and temperature fields of rectangular jets," *International Journal of Heat and Mass Transfer* **19**(11), 1289-1297, (1976). [https://doi.org/10.1016/0017-9310\(76\)90081-8](https://doi.org/10.1016/0017-9310(76)90081-8)
- ²³ D.B. Spalding, "Turbulent Jets. N. Rajaratnam. Elsevier Scientific Publishing Company, Amsterdam," *International Journal of Heat and Mass Transfer* **20**(3), (1977). <https://doi.org/10.1017/S001924000034540>
- ²⁴ R.C. Deo, J. Mi, and G.J. Nathan, "The influence of nozzle aspect ratio on plane jets," *Experimental Thermal and Fluid Science* **31**(8), 825-838, (2007). <https://doi.org/10.1016/j.expthermflusci.2006.08.009>
- ²⁵ W.R. Quinn, "Turbulent free jet flows issuing from sharp-edged rectangular slots: The influence of slot aspect ratio," *Experimental Thermal and Fluid Science* **5**(2), 203-215, (1992). [https://doi.org/10.1016/0894-1777\(92\)90007-R](https://doi.org/10.1016/0894-1777(92)90007-R)
- ²⁶ Y. Tsuchiya, and C. Horikoshi, "On the spread of rectangular jets," *Experiments in Fluids* **4**(4), 197-204, (1986). <https://doi.org/10.1007/BF00717815>
- ²⁷ A.K.M.F. Hussain, and A.R. Clark, "Upstream influence on the near field of a plane turbulent jet," *Physics of Fluids* **20**(9), 1416–1426 (1977). <https://doi.org/10.1007/BF00717815>
- ²⁸ G.P. Lemieux, and P.H. Oosthuizen, "Experimental study of the behaviour of plane turbulent jets at low Reynolds numbers," *AIAA Journal* **23**(12), 1845-1846 (1985). <https://doi.org/10.2514/3.9183>
- ²⁹ I. Namer, and M. V. Ötügen, "Velocity measurements in a plane turbulent air jet at moderate Reynolds numbers," *Experiments in Fluids* **6**(6), 387-399, (1988). <https://doi.org/10.1007/bf00196484>
- ³⁰ R.C. Deo, J. Mi, and G.J. Nathan, "The influence of Reynolds number on a plane jet," *Physics of Fluids* **20**(7), 075108 (2008). <https://doi.org/10.1063/1.2959171>
- ³¹ R.C. Deo, G.J. Nathan, and J. Mi, "Similarity analysis of the momentum field of a subsonic, plane air jet with varying jet-exit and local Reynolds numbers," *Physics of Fluids* **25**(1), 015115 (2013). <https://doi.org/10.1063/1.4776782>
- ³² G.J. Hitchman, A.B. Strong, P.R. Slawson, and G.D. Ray, "Turbulent plane jet with and without confining end walls," *AIAA Journal* **28**(10), 1699–1700 (1990). <https://doi.org/10.2514/3.10460>
- ³³ M. Alnahhal, A. Cavo, A. Romeos, K. Perrakis, and T. Panidis, "Experimental investigation of the effect of endplates and sidewalls on the near field development of a smooth contraction rectangular jet," *European Journal of Mechanics, B/Fluids* **30**(4), 451-465, (2011). <https://doi.org/10.1016/j.euromechflu.2011.04.003>
- ³⁴ J. Bridges, and M.P. Wernet, "Turbulence measurements of rectangular nozzles with bevel," in *53rd AIAA Aerospace Sciences Meeting*, (2015). <https://doi.org/10.2514/6.2015-0228>
- ³⁵ T. KIWATA, S. KIMURA, N. KOMATSU, H. MURATA, and Y.H. KIM, "Flow Characteristics of a Plane Jet with an Extended Lip-Plate and Serrated Tabs," *Journal of Fluid Science and Technology* **4**(2), 268-278, (2009). <https://doi.org/10.1299/jfst.4.268>

- 764 ³⁶ K. HIRATA, K. SHOBU, T. MURAYAMA, and J. FUNAKI, "Flow Characteristics of Plane Jet from an Asymmetrical
 765 Two-Dimensional Nozzle," *Journal of Environment and Engineering* **5**(1), 183-199, (2010).
 766 <https://doi.org/10.1299/jee.5.183>
- 767 ³⁷ J.Y. Kwak, and Y. Lee, "An experimental study on the characteristics of rectangular supersonic jet on a flat plate,"
 768 *International Journal of Aeronautical and Space Sciences* **17**(3), 324-331, (2016).
 769 <https://doi.org/10.5139/IJASS.2016.17.3.324>
- 770 ³⁸ C. Jente, "Engine integration of high aspect ratio rectangular jet nozzle (unheated subsonic flow)," in *28th AIAA/CEAS Aeroacoustics Conference*, (2022). <https://doi.org/10.2514/6.2022-2869>
- 771 ³⁹ A. Dolai, P. Boggavarapu, N. Swaminathan, and R. V. Ravikrishna, "Vortex breakdown modes in co/counter-swirling
 772 non-reacting and reacting flows," *Phys. Fluids* **37**, 025212 (2025). <https://doi.org/10.1063/5.0253056>
- 773 ⁴⁰ M. Kuhnhenn, T. V. Joensen, M. Reck, I. V. Roisman, and C. Tropea, "Study of the internal flow in a rotary atomizer
 774 and its influence on the properties of the resulting spray," *International Journal of Multiphase Flow* **100**, 30-40, (2018).
 775 <https://doi.org/10.1016/j.ijmultiphaseflow.2017.11.019>
- 776 ⁴¹ H. Görtler, "Berechnung von Aufgaben der freien Turbulenz auf Grund eines neuen Näherungsansatzes ..," *ZAMM -
 777 Journal of Applied Mathematics and Mechanics / Zeitschrift Für Angewandte Mathematik Und Mechanik* **22**(5), 244-254,
 778 (1942). <https://doi.org/10.1002/zamm.19420220503>
- 779 ⁴² L.J.S. Bradbury, "The structure of a self-preserving turbulent plane jet," *Journal of Fluid Mechanics* **23**(1), 31-64,
 780 (1965). <https://doi.org/10.1017/S0022112065001222>
- 781 ⁴³ -W. Tollmien, "Calculation of Turbulent Expansion Processes," *NACA TM-1085 (National Advisory Committee for
 782 Aeronautics, Langley Field, VA)* **6**, (1945). <http://catalog.hathitrust.org/Record/012183098>
- 783 ⁴⁴ X. An, B. Dong, Y. Zhang, Y. Wang, X. Zhou, and W. Li, "Influence of the wettability on the liquid breakup in planar
 784 prefilming airblast atomization using a coupled lattice Boltzmann-large eddy simulation model," *Physics of Fluids* **34**(5),
 785 053302 (2022). <https://doi.org/10.1063/5.0088648>
- 786 ⁴⁵ A. Kumar, and S. Sahu, "Liquid jet breakup unsteadiness in a coaxial air-blast atomizer," *International Journal of
 787 Spray and Combustion Dynamics* **10**(3), 211-230, (2018). <https://doi.org/10.1177/1756827718760905>
- 788 ⁴⁶ K. Warncke, S. Gepperth, B. Sauer, A. Sadiki, J. Janicka, R. Koch, and H.J. Bauer, "Experimental and numerical
 789 investigation of the primary breakup of an airblasted liquid sheet," *International Journal of Multiphase Flow* **91**, 208-
 790 224, (2017). <https://doi.org/10.1016/j.ijmultiphaseflow.2016.12.010>
- 791 ⁴⁷ X. An, B. Dong, Y. Zhang, F. Geng, X. Zhou, Y. Qin, and W. Li, "Effects of structured prefilmer lip on spray
 792 characteristics in planar prefilming airblast atomization," *Aerospace Science and Technology* **140**, 108426 (2023).
 793 <https://doi.org/10.1016/j.ast.2023.108426>
- 794 ⁴⁸ F. Vashahi, R.A. Dafsari, S. Rezaei, J.K. Lee, and B.J. Baek, "Assessment of steady VOF RANS turbulence models in
 795 rendering the internal flow structure of pressure swirl nozzles," *Fluid Dynamics Research* **51**(4), 045506 (2019).
 796 <https://doi.org/10.1088/1873-7005/ab2546>
- 797 ⁴⁹ M.M. Tareq, R.A. Dafsari, S. Jung, and J. Lee, "Effect of the physical properties of liquid and air on the spray
 798 characteristics of a pre-filming airblast nozzle," *International Journal of Multiphase Flow* **126**, 103240 (2020).
 799 <https://doi.org/10.1016/j.ijmultiphaseflow.2020.103240>
- 800 ⁵⁰ R.A. Dafsari, H.J. Lee, J. Han, D.C. Park, and J. Lee, "Viscosity effect on the pressure swirl atomization of an alternative
 801 aviation fuel," *Fuel* **240**, 179-191, (2019). <https://doi.org/10.1016/j.fuel.2018.11.132>
- 802 ⁵¹ M. K. Kasbi, R. A. Dafsari, A. Charanandeh, J. Kim, and J. Lee, "On the Generation of Coanda Flow with Influential
 803 Parameters in Coaxial Triple Swirler," *Atomization and Spray*, vol. 34, pp. 1-28, (2024).
 804 <https://doi.org/10.1615/atomizspr.2023048227>
- 805 ⁵² B.R. Ramaprian, and M.S. Chandrasekhara, "LDA measurements in plane turbulent jets," *Journal of Fluids
 806 Engineering, Transactions of the ASME* **107**(2), 264-271, (1985). <https://doi.org/10.1115/1.3242472>
- 807 ⁵³ K. Khani Aminjan, M. Ghodrat, M. Heidari, A. Arjmandfar, P. Rahamanivahid, R.D. Cosme Pecho, Y. Yasin, and S.
 808 Shukhratovich Abdullaev, "Study on duplex air-blast atomizers spray in the engine real operation conditions," *Physics of
 809 Fluids* **35**(7), 073326 (2023). <https://doi.org/10.1063/5.0153468>
- 810 ⁵⁴ A. H. Lefebvre and D. Miller, "The Development of an Air Blast Atomizer for Gas Turbine Application," *Report at
 811 College of Aeronautics, Cranfield, UK*, (1966). <https://resolver.tudelft.nl/uuid:dc6f3869-2d7e-427d-95c7-2ea1df7ade35>
- 812 ⁵⁵ I. Oshima, and A. Sou, "Air-blast atomization of a liquid film," *Journal of Fluid Mechanics* **985**, A36, (2024).
 813 <https://doi.org/10.1017/jfm.2024.279>
- 814 ⁵⁶ Y. Liao, S.M. Jeng, M.A. Jog, and M.A. Benjamin, "Advanced sub-model for airblast atomizers," *Journal of Propulsion
 815 and Power* **17**(2), 411-417, (2001). <https://doi.org/10.2514/2.5757>
- 816 ⁵⁷ M. Roudini, and G. Wozniak, "Experimental investigation of spray characteristics of pre-filming Air-blast atomizers,"
 817 *Journal of Applied Fluid Mechanics* **11**(6), 1455-1469, (2018). <https://doi.org/10.29252/jafm.11.06.28115>
- 818 ⁵⁸ C.M. Or, K.M. Lam, and P. Liu, "Potential core lengths of round jets in stagnant and moving environments," *Journal
 819 of Hydro-Environment Research* **5**(2), 81-91, (2011). <https://doi.org/10.1016/j.jher.2011.01.002>
- 820 ⁵⁹ W.R. Quinn, and M. Azad, "Mean streamwise centerline velocity decay and entrainment in triangular and circular jets,"
 821 *AIAA Journal* **51**(1), 70-79, (2013). <https://doi.org/10.2514/1.J051559>
- 822 ⁶⁰ S. Park, and M. Lee, "A semi-supervised framework for analyzing the potential core of a low-density jet," *Flow
 823 Measurement and Instrumentation* **95**, 102516 (2024). <https://doi.org/10.1016/j.flowmeasinst.2023.102516>
- 824 ⁶¹ S. Sharma, M. Klein, and H. Schmidt, "Features of far-downstream asymptotic velocity fluctuations in a round jet: A
 825 one-dimensional turbulence study," *Physics of Fluids* **34**(8), 085134 (2022). <https://doi.org/10.1063/5.0101270>

- 827 ⁶² M.J. Lighthill, "Jet noise," *AIAA Journal* **1**(7), 1507–1517, (1963). <https://doi.org/10.2514/3.1848>
- 828 ⁶³ F.O. Thomas, and V.W. Goldschmidt, "Structural characteristics of a developing turbulent planar jet," *Journal of Fluid Mechanics* **163**, 227-256, (1986). <https://doi.org/10.1017/S0022112086002288>
- 829 ⁶⁴ N.T. Obot, M.L. Graska, and T.A. Trabold, "The near field behavior of round jets at moderate reynolds numbers," *Canadian Journal of Chemical Engineering* **62**(5), 587-593, (1984). <https://doi.org/10.1002/cjce.5450620503>
- 830 ⁶⁵ S.H. Hassan, T. Guo, and P.P. Vlachos, "Flow field evolution and entrainment in a free surface plunging jet," *Physical Review Fluids* **4**(10), 104603 (2019). <https://doi.org/10.1103/PhysRevFluids.4.104603>
- 831 ⁶⁶ B. Khorsandi, S. Gaskin, and L. Mydlarski, "Effect of background turbulence on an axisymmetric turbulent jet," *Journal of Fluid Mechanics*, **736**, 250–286, (2013). <https://doi.org/10.1017/jfm.2013.465>
- 832 ⁶⁷ D. R. Miller and E. W. Comings, Static Pressure Distribution in the Free Turbulent Jet, *Journal of Fluid Mechanics*, **3**, 1–16, (1957). <https://doi.org/10.1017/S0022112057000440>
- 833 ⁶⁸ L. Wang, and L.H. Feng, "Extraction and reconstruction of individual vortex-shedding mode from bistable flow," *AIAA Journal* **55**(7), 2129-2141, (2017). <https://doi.org/10.2514/1.J055306>
- 834 ⁶⁹ J. Li, B. Wang, X. Qiu, J. Wu, Q. Zhou, S. Fu, and Y. Liu, "Three-dimensional vortex dynamics and transitional flow induced by a circular cylinder placed near a plane wall with small gap ratios," *Journal of Fluid Mechanics*, **953**, A2, (2022). <https://doi.org/10.1017/jfm.2022.930>
- 835 ⁷⁰ K. Steiros, M. Obligado, P. Bragança, C. Cuvier, and J.C. Vassilicos, "Turbulent shear flow without vortex shedding, Reynolds shear stress and small-scale intermittency," *Journal of Fluid Mechanics*, **1002**, A51, (2025). <https://doi.org/10.1017/jfm.2024.1197>
- 836 ⁷¹ H. Huang, M. Chen, X. Ma, D. Wang, L. Yang, and X. Zhou, "Experimental study of the Reynolds stress distribution and its self-similarity in a semi-confined impinging jet," *Ocean Engineering*, **289**, 116163 (2023). <https://doi.org/10.1016/j.oceaneng.2023.116163>
- 837 ⁷² H. Fellouah, C.G. Ball, and A. Pollard, "Reynolds number effects within the development region of a turbulent round free jet," *International Journal of Heat and Mass Transfer*, **52**(17–18), 3943-3954 (2009). <https://doi.org/10.1016/j.ijheatmasstransfer.2009.03.029>
- 838 ⁷³ P. A. Durbin, "Advanced Approaches in Turbulence: Theory, Modeling, Simulation, and Data Analysis for Turbulent Flows," *Elsevier, Amsterdam*, (2021). <https://doi.org/10.1016/C2019-0-01450-1>
- 839 ⁷⁴ X. Zhou, H. Huang, Y. Hu, M. Chen, L. Yang, and P. Jiang, "Turbulent structures and associated Reynolds shear stress in an impinging jet," *International Journal of Heat and Mass Transfer*, **244**, 109264 (2025). <https://doi.org/10.1016/j.ijheatmasstransfer.2025.126948>
- 840 ⁷⁵ J. Weiss, "A tutorial on the proper orthogonal decomposition," in AIAA Aviation 2019 Forum, (2019). <https://doi.org/10.2514/6.2019-3333>
- 841 ⁷⁶ M.A. Nikolaidis, P.J. Ioannou, B.F. Farrell, and A. Lozano-Durán, "POD-based study of turbulent plane Poiseuille flow: comparing structure and dynamics between quasi-linear simulations and DNS," *Journal of Fluid Mechanics*, **962**, A16, (2023). <https://doi.org/10.1017/jfm.2023.274>
- 842 ⁷⁷ S.C. Crow, and F.H. Champagne, "Orderly structure in jet turbulence," *Journal of Fluid Mechanics*, **48**(3), 547-591, (1971). <https://doi.org/10.1017/S0022112071001745>
- 843 ⁷⁸ H.J. Hussein, S.P. Capp, and W.K. George, "Velocity measurements in a high-Reynolds-number, momentum-conserving, axisymmetric, turbulent jet," *Journal of Fluid Mechanics*, **258**, 31-75, (1994). <https://doi.org/10.1017/S002211209400323X>